Monthly Notices of the ROYAL ASTRONOMICAL SOCIETY

MNRAS **536,** 3707–3738 (2025) https://doi.org/10.1093/mnras/stae2797
Advance Access publication 2024 December 20

VIRAC2: NIR astrometry and time series photometry for 500M+ stars from the VVV and VVVX surveys

Leigh C. Smith,[1]★ Philip W. Lucas,[2] Sergey E. Koposov,[1,3,4] Carlos Gonzalez-Fernandez,[1] Javier Alonso-García,[5,6] Dante Minniti,[7,8] Jason L. Sanders,[9] Luigi R. Bedin,[10] Vasily Belokurov,[1] N. Wyn Evans,[1] Maren Hempel,[7,11] Valentin D. Ivanov,[12] Radostin G. Kurtev[13,14] and Roberto K. Saito[15]

[1]*Institute of Astronomy, University of Cambridge, Madingley Road, Cambridge CB3 0HA, UK*
[2]*Centre for Astrophysics Research, University of Hertfordshire, College Lane, Hatfield AL10 9AB, UK*
[3]*Institute for Astronomy, University of Edinburgh, Royal Observatory, Blackford Hill, Edinburgh EH9 3HJ, UK*
[4]*Kavli Institute for Cosmology, University of Cambridge, Madingley Road, Cambridge CB3 0HA, UK*
[5]*Centro de Astronomía (CITEVA), Universidad de Antofagasta, Av. Angamos 601, Antofagasta, Chile*
[6]*Millennium Institute of Astrophysics, Nuncio Monseñor Sotero Sanz 100, Office 104, Providencia, Santiago, Chile*
[7]*Instituto de Astrofísica, Dep. de Ciencias Físicas, Facultad de Ciencias Exactas, Universidad Andres Bello, Av. Fernández Concha 700, Santiago, Chile*
[8]*Vatican Observatory, Specola Vaticana, V-00120, Vatican City, Vatican City State*
[9]*Department of Physics and Astronomy, University College London, London WC1E 6BT, UK*
[10]*INAF - Osservatorio Astronomico di Padova, Vicolo dell'Osservatorio 5, Padova I-35122, Italy*
[11]*Max-Planck Institute for Astronomy, Königstuhl 17, D-69117 Heidelberg, Germany*
[12]*European Southern Observatory, Karl-Schwarzschild-Str. 2, D-85748 Garching bei München, Germany*
[13]*Instituto de Física y Astronomía, Universidad de Valparaíso, Av. Gran Bretaña 1111, Playa Ancha, Valparaíso, Chile*
[14]*The Millennium Institute of Astrophysics (MAS), Av. Vicuña Mackenna 4860, 782-0436 Macul, Santiago, Chile*
[15]*Departamento de Física, Universidade Federal de Santa Catarina, Trindade 88040-900, Florianópolis, Brazil*

Accepted 2024 December 18. Received 2024 December 18; in original form 2024 July 5

ABSTRACT

We present VIRAC2, a catalogue of positions, proper motions, parallaxes and Z, Y, J, H, and K_s near-infrared photometric time series of 545 346 537 unique stars. The catalogue is based on a point spread function fitting reduction of nearly a decade of VISTA VVV and VVVX images, which cover 560 deg^2 of the Southern Galactic plane and bulge. The catalogue is complete at the $>$ 90 per cent level for $11 < K_s$ mag < 16 sources, but extends to $K_s \approx 17.5$ mag in most fields. Astrometric performance for $11 < K_s$ mag < 14 sources is typically ≈ 0.37 mas yr^{-1} per dimension for proper motion, and 1 mas for parallax. At $K_s = 16$ the equivalent values are around 1.5 mas yr^{-1} and 5 mas. These uncertainties are validated against *Gaia* DR3 and *Hubble Space Telescope* astrometry. The complete catalogues are available via the ESO archive. We perform an initial search of the catalogue for nearby ultracool dwarf candidates. In total, we find 26 new sources whose parallaxes place them within 50 parsecs of the Sun. Among them we find two high-confidence T dwarfs and a number of other sources that appear to lie close to the L/T transition.

Key words: parallaxes – proper motions – brown dwarfs – stars: kinematics and dynamics – Galaxy: kinematics and dynamics – solar neighbourhood.

1 INTRODUCTION

The VISTA Variables in the Via Lactea (VVV; Minniti et al. 2010) is a near-infrared multiepoch photometric survey conducted using the VISTA telescope at the Paranal Observatory, Chile. It observed 560 deg^2 of the bulge and southern disc of the Milky Way between 2009 and 2015, and comprises roughly a hundred epochs in the K_s bandpass at a typical pointing, with additional epochs in Z, Y, J, and H bandpasses at the beginning and end of the survey. The recently completed VVV extended survey (VVVX; Saito et al. 2024) built on the VVV survey by extending the area coverage to 1700 deg^2 in the J, H, and K_s bandpasses. It also included many additional epochs for the VVV survey area, extending the time baseline by more than a factor of 2.

The bulge and disc comprise the vast majority of the resolvable stellar content of the Milky Way; fertile ground for a great number of subfields of stellar and galactic astronomy. One obvious use of the VVV and VVVX time series data covering this region is the measurement of stellar proper motions. In this context, the data sets remain useful even in the *Gaia* era due to their ability to survey deeper into regions of high Galactic extinction (see e.g. Smith et al. 2018, fig. 4). Several previous works have made proper motion measurements within subsections of the VVV data (e.g. Libralato et al. 2015; Contreras Ramos et al. 2017; Griggio et al. 2024).

The VVV Infrared Astrometric Catalogue (VIRAC v1 hereafter; Smith et al. 2018) capitalized on the original VVV survey, providing proper motion measurements from the time sequence observations

★ E-mail: lsmith@ast.cam.ac.uk

of some 300 million unique sources over 5 yr. Additionally, for around 7000 objects that exhibited large proper motions it provided parallax measurements at $> 5\sigma$. At the time, the lack of suitable astrometric reference catalogues meant that astrometric calibration had to be performed in a *relative* sense, i.e. measured motions of individual stars were relative to those of the nearby field. This was a major drawback of VIRAC v1, e.g. for the purposes of large-scale studies of the motions of Milky Way stars. Shortly after VIRAC v1 was published, the second data release of the *Gaia* survey became available. Some authors (Clarke et al. 2019; Sanders et al. 2019) capitalized on this by performing their own recalibration of VIRAC v1 (designated VIRAC v1.1 in the Sanders et al. 2019 case) in order to study the kinematic properties of the Galactic bar, though these catalogue versions were never made available publicly.

VIRAC v1 was built from the aperture photometric catalogues provided by the Cambridge Astronomical Survey Unit (CASU). These data products are superb for observations with limited blending, but do suffer from source confusion in regions of significant stellar crowding. The VVV and VVVX surveys cover regions of the Milky Way with the highest stellar densities, in infrared bandpasses that are less impacted by the effects of interstellar reddening, and hence are subject to significant source confusion. Point source profile fitting photometry is usually better suited to such observations (Stetson 1987).

Smith et al. (2018) described their planned version two of VIRAC, based on profile fitting photometry, and using *Gaia* as an external reference catalogue. This paper describes the VIRAC version 2 (VIRAC2 hereafter) pipeline and catalogue. In addition to the above enhancements, VIRAC2 includes more observations, covering a longer time baseline; it incorporates an image-level astrometric calibration algorithm that used *Gaia* DR3 (and its reduced systematic errors relative to *Gaia* DR2) as an external reference catalogue; and it benefits from a global photometric calibration algorithm, with a secondary component designed to reduce high-frequency atmosphere-induced photometric scatter.

This paper is organized as follows. In Section 2, we describe the data, source detection, astrometric and photometric calibration algorithms, and the main VIRAC2 pipeline. In Section 3, we describe the catalogues, the steps taken to clean them, validate their contents against external sources, and demonstrate how they may be accessed. In Section 4, we outline and present the results of searches within the catalogues for new nearby sources such as brown dwarfs and white dwarfs that are either too optically faint for *Gaia* or otherwise overlooked. Such sources are of interest in order to complete the census of systems in nearby space, enabling a better understanding of star formation and stellar evolution. These searches add to previous VVV-based searches for brown dwarfs and high proper motion stars (Beamín et al. 2013; Ivanov et al. 2013; Smith et al. 2015; Kurtev et al. 2017; Smith et al. 2018) and earlier searches in the Galactic plane based on other data sets, e.g. Folkes et al. (2007), Looper, Kirkpatrick & Burgasser (2007), Phan-Bao et al. (2008), Lucas et al. (2010), Burningham et al. (2011), Folkes et al. (2012), Smith et al. (2014), and many more. We show that ground-based near infrared searches continue to be valuable in the era of *Gaia* (Prusti et al. 2016) and the *Wide Field Survey Explorer* (*WISE*; Wright et al. 2010) despite the leading role now played by those two all-sky survey missions.

2 DATA AND METHODS

The data flow for VIRAC2, from reduced images to astrometrically and photometrically calibrated source lists and time series, comprised multiple fairly distinct components. In order, they were: source detection, astrometric calibration, stellar time series production and mean astrometry fitting, and photometric calibration.

The VIRAC2 pipeline went through a number of design iterations during development. One version, internally designated VIRAC2β, produced a completed catalogue that was used in a number of published articles (e.g. Alonso-García et al. 2021; Husseiniova et al. 2021; Minniti et al. 2021; Smith et al. 2021; Kaczmarek et al. 2022; Molnar et al. 2022; Peña Ramírez et al. 2022; Sormani et al. 2022; Sanders et al. 2022a, b; Kaczmarek et al. 2024; Lucas et al. 2024; Luna et al. 2024; Minniti et al. 2024; Nieuwmunster et al. 2024; Sanders et al. 2024, to name a few). In addition to those works, it was used at various points during the final catalogue production, primarily the photometric calibration component (see Section 2.5), and as a seed catalogue for the source list of the main pipeline (see Section 2.4.1). Since this earlier pipeline and catalogue influenced the final versions, for completeness we describe the main differences between the VIRAC2β and final VIRAC2 pipeline versions in Appendix A.

2.1 Data

The recently retired VISTA Infrared Camera (VIRCAM) was the largest near-infrared detector array ever used for astronomy, with sixteen 2048×2048 pixel arrays. VISTA and VIRCAM image a total area of 0.6 deg^2 at each pointing position or 'pawprint'. Detectors are arranged in a 4×4 grid with spacings of 90 per cent of a detector width in the Y dimension and 42.5 per cent of a detector width in the X dimension. The conventional VIRCAM tiling pattern consists of six of these pawprints (three offset in X and two in Y) that fill a VIRCAM 'tile' when stacked. VIRCAM tiles are approximately $1.4^\circ \times 1.1^\circ$. Most positions in a VIRCAM tile are observed twice due to the ≈ 50 per cent pawprint overlap in the X-direction. VISTA and VIRCAM are described by Sutherland et al. (2015). CASU provide pipeline data reduction and calibration of the photometry and astrometry via the VISTA Data Flow Pipeline (Irwin et al. 2004), see also Lewis, Irwin & Bunclark (2010) and http://casu.ast.cam.ac.uk/surveys-projects/vista/technical.

From CASU we acquired 179 403 VVV, and 18 020 VVVX observations (pawprints) that cover the VVV area. Pawprints, rather than tile stacks, should be used for precise astrometric work (Alonso-García et al. 2018). The process of stacking to produce tiles complicates the point spread function (PSF) and background estimation. The observations spanned 2010 January 30 to 2019 September 1 and passed our basic quality control cuts – images with incomplete FITS headers, seeing > 2.0 arcsec, source count $<20\,000$, or sky level as determined by IMCORE[1] > 2000 counts per second were rejected.

2.2 Source detection and preliminary processing

Source detection and photometry was performed in an automated manner using a version of DoPHOT (Schechter, Mateo & Saha 1993; Alonso-García et al. 2012), developed to perform PSF photometry extraction on highly crowded photometric images. Alonso-García et al. (2018) demonstrated that it is capable of detecting a significantly higher proportion of stars in VVV fields. Further modification was undertaken by ourselves in order to extract astrometric uncertainties. DoPHOT produced 1.14×10^{11} tentative source detections from the 197 423 images.

[1]Irwin (1985); http://casu.ast.cam.ac.uk/surveys-projects/software-release/imcore

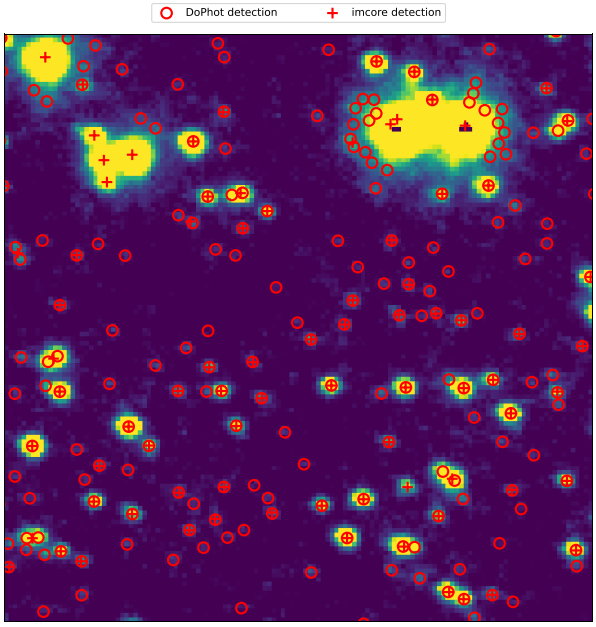

Figure 1. CASU IMCORE versus DoPHOT source detections for an example image cut-out, selected to showcase the strengths and weaknesses of each algorithm. DoPHOT detections are plotted as red circles, and IMCORE detections are plotted as red pluses. DoPHOT is prone to erroneous detection of sources in the wings of bright stars and fails to detect saturated ones, but it is better able to separate blends and has a fainter detection limit. IMCORE detections tend to map consistently to real stars and saturated ones are recovered more reliably, though it deblends less effectively and has a brighter upper detection limit.

VIRAC version 1 was based on source catalogues provided by CASU. These were produced by processing the VVV images with their aperture reduction software, IMCORE. The VVV and VVVX surveys cover the regions of the sky with the highest Galactic stellar density in the near infrared, and as such suffer from significant blending. Since DoPHOT uses PSF fitting, it is better suited to analysis of these heavily blended fields. A comparison of the IMCORE and DoPHOT source detection algorithms for an example image cut-out is provided in Fig. 1. This cut-out covers the region $1088 < X < 1220$, $1910 < Y < 2042$ of detector 1 from exposure v20120621_00300_st. It was selected purely to showcase the strengths and weaknesses of each algorithm, although being nearly 5 deg from the Galactic Centre it is not a particularly dense field in VVV terms (centred on $l, b = 356.0, -2.8$). DoPHOT has poor saturated star detection performance relative to IMCORE. Across the top half of the image we see multiple saturated (left) or highly saturated (right) stars that DoPHOT fails to detect. This is partly an artificial restriction, since DoPHOT is unable to reliable fit the fluxes of saturated objects it typically masks them instead. Additionally, Fig. 1 shows that with our run configuration DoPHOT erroneously detects sources in the wings of the highly saturated stars. This was also a conscious choice, since close companions to bright stars can be interesting and should ideally be kept. By contrast, IMCORE quite reliably detects saturated stars and it shows little contamination by false detections. Across the lower half of the cut-out, there are several instances where blended stars are reliably deblended by DoPHOT but not by IMCORE. It is also evident that DoPHOT detects many more stars than IMCORE at the fainter end, but some of these are erroneous detections of peaks in sky noise. Again, this is partly driven by our run configuration, which was tuned to push the faint limit. We ultimately utilized the multiple epochs to identify and remove the erroneous detections.

CASU provide 2d arrays mapping detector sensitivity (confidence maps) for every VIRCAM image. We recorded the confidence map value of the pixel containing the centroid of each detected source. One dither contributes ≈ 50 to confidence, so regions of the detector covered by both dithers have confidence of ≈ 100. Sources detected in image regions with confidence < 25 were rejected. This most frequently occurs for sources in regions where a defective portion of a chip is not covered by the second dither position, or a where a source is covered by a defective region of the chip in both dither positions. We applied the CASU astrometric solution and radial distortion correction to each array in the catalogue to produce equatorial coordinates. The CASU astrometric solution was based on array positions measured by IMCORE. We did not necessarily expect IMCORE centroids to agree exactly with the DoPHOT centroids, but they were sufficiently close that the astrometric solution was still valid for preliminary processing purposes. At this stage, we simply required equatorial coordinates precise enough to identify sources in common with our astrometric reference catalogue.

2.3 Astrometric calibration of individual images

As our astrometric reference catalogue we used the projected position of *Gaia* DR3 sources at the epoch of the VISTA observation, taking into account their proper motions and parallaxes ($\alpha\delta_{Gaia}$ hereafter). Of the *Gaia* reference sources, we simply required a full five-parameter astrometric solution and renormalized unit weight error (ruwe) < 1.4, to reject sources with poorly behaved astrometric solutions (e.g. binary stars; Lindegren et al. 2018, 2021; Stassun & Torres 2021). Of the VISTA detections, we required that reference sources were 'perfect' stars according to DoPHOT, i.e. they were fitted using the full seven parameter (sky level, flux, position, and shape) model.

While matching between the VISTA and reference catalogues we found in some cases that the CASU astrometric solution was systematically offset from $\alpha\delta_{Gaia}$ in portions of the detector by up to 300 mas. As a result, it was necessary to first refine the CASU astrometry by fitting a simple six parameter linear transformation matrix to align the two coordinate systems using sources matched within 1 arcsec. After this, to produce a final pool of astrometric reference sources we cross-matched the $\alpha\delta_{Gaia}$ catalogue to the VISTA catalogues with a 0.25 arcsec matching radius.

The $\alpha\delta_{Gaia}$ positions of the reference sources were then TAN projected using a tangent point at the centre of the VIRCAM focal plane given in the FITS header of the original VISTA image. The resultant tangent plane coordinates were the $\chi\eta_{Gaia}$ astrometric reference frame.

We fitted Chebyshev polynomials of varying degree to map reference source VIRCAM array coordinate positions to their $\chi\eta_{Gaia}$ coordinates. This approach was found to perform well in our many test fields, while also limited overfitting in regions with relatively few *Gaia* reference sources.

For each chip of each observation we measured residuals to least squares fits of increasing degrees of Chebyshev polynomials using fivefold cross-validation. The sequence of polynomial degrees tested was: 3, 4, 5, 6, 7, 8, 10, and 13. At the point that the standardized cross-validated residuals began to deteriorate, the previous value was determined to be optimal to avoid overfitting and the testing sequence was terminated. Once the optimal value was determined, reference sources with a residual in either dimension greater than 10σ were

removed and a final re-fitting of Chebyshev polynomial coefficients was performed.

Our treatment of positional uncertainties began with a formal propagation of the array coordinate uncertainties reported by DoPhot through the Chebyshev polynomial fitted in the previous stage, to obtain uncertainties in the $\chi\,\eta_{Gaia}$ reference frame. Rather than explicitly incorporating the uncertainties on the Chebyshev polynomial coefficients themselves, we elected to fit for calibration uncertainties to be added in quadrature and also a multiplicative scaling factor to be applied to the uncertainties reported by DoPhot. I.e.:

$$\sigma^2_{\rm VISTA} = \sigma^2_{\rm cal} + l\,\sigma^2_{\rm DoPhot} \tag{1}$$

where $\sigma_{\rm cal}$ and l are the calibration uncertainties and error scaling factor, respectively.

For each dimension, over N equal width magnitude bins we minimized the function:

$$\sum_{n=1}^{N}\left(\ln\left(k\cdot{\rm MAD}\left(r\cdot\sqrt{\sigma^2_{Gaia}+\sigma^2_{\rm VISTA}}\right)\right)\right)^2, \tag{2}$$

where k is the 1.4826 approximate scaling factor to be applied to the median absolute deviation (MAD) to obtain a reasonable estimate of the standard deviation that is robust against outliers, and r are the separations between the transformed VISTA coordinates and *Gaia* coordinates in a given dimension.

The objective was to rescale the uncertainties such that the residual to the coordinate transformation divided by its uncertainty was approximately unit Gaussian. By measuring the spread within sets of equal width magnitude bins we avoided the fainter magnitude bins having undue weight due to their significantly larger source volume. The obtained calibration uncertainty and error scaling factors were applied to the DoPhot positional uncertainties as per equation (1) to obtain our final single-epoch positional uncertainties.

2.4 Catalogue pipeline

The main catalogue production pipeline can be summarized as an iterative process of two main components: source matching and astrometric fitting. Ultimately, the goal of this iterative procedure was to produce a complete list of sources, having correctly identified their corresponding detections in each VISTA observation. Individual healpixels of resolution 8–10 (approximately 189, 47, or 12 square arcmin, chosen based on approximate local source density and epoch count) were processed independently, incorporating a small border to include detections of sources straddling the edges of the target healpixel.

2.4.1 Initial source matching

The first step (after data ingestion, etc.) was to perform an initial source matching, producing a complete but highly contaminated (by duplicates, noise, etc.) source list (SL hereafter). The SL was seeded with the VIRAC2β catalogue, which in turn had been seeded with *Gaia* DR2 (see Appendix A for more details).

The positions of SL sources were propagated to the epoch of the first (chronological) VISTA catalogue using their five-parameter astrometric solutions. The propagated positions were then matched to the VISTA catalogue with a 0.339 arcsec radius (the average VIRCAM pixel size), requiring each match to be the best match in both directions and also within a radius of five times the positional uncertainty. VISTA catalogue row indices of successful matches were recorded for each SL row. The requirement that a match is the best in both directions at this stage implies that multiple SL sources cannot be associated with a single VISTA catalogue detection. Unmatched VISTA catalogue rows were then appended to the SL, and at this stage they were assigned proper motion and error in each dimension equal to the mean and standard deviation of the proper motions of VIRAC2β seed sources within the same healpixel, and a parallax of 0.0 mas and uncertainty equal to the standard deviation of the parallaxes of the seed sources. Not taking the local proper motion distribution into account is equivalent to assuming zero proper motion, which is generally incorrect and could become important when cross-matching with large epoch differences. Since the majority of sources in this bandpass, depth and direction are located in the vicinity of the Galactic Centre, at ≈ 8 kpc, only a small fraction will have parallax greater than a few tenths of a milliarcsecond. An error of even a few milliarcseconds is at the level of a few per cent of the matching radius, which we deemed acceptable, particularly as it is only an initial guess.

This matching procedure then continued for each VISTA observation in chronological order until our complete but contaminated SL was produced. SL rows with fewer than two contributing VISTA detections were removed.

2.4.2 Astrometric fitting

With sequences of VISTA detections for each source, we read their K_s astrometric time series and fitted their five astrometric parameters. We used only the K_s bandpass data for astrometry fitting. For sources with fewer than 10 epochs we simply calculated a mean position, epoch and positional uncertainty, and assumed they had the average proper motion of local VIRAC2β sources and zero parallax (as in Section 2.4.1). For sources with 10 or more epochs we proceeded with a full five-parameter least squares astrometric solution as described below. We worked in local tangent plane coordinates: the astrometric time series for each source underwent a TAN projection to a χ and η reference system about its mean equatorial position, yielding positional offsets equivalent to $\Delta\alpha\cos\delta$ and $\Delta\delta$.

We measured preliminary residuals to the five-parameter astrometric model (χ_0, η_0, ω, μ_χ, and μ_η) by least squares fitting the astrometric time series using fivefold cross-validation, using their inverse variances (see Section 2.3) as weights. Model parameters were fixed at the reference epoch, 2014.0, chosen to be the approximate midpoint of the survey. Observations with $> 5\sigma$ residuals were removed and if there were still ≥ 10 remaining observations then the astrometric model fitting was repeated without cross-validation. The resulting astrometric solution, including its covariance matrix, is recorded and residuals to it are remeasured and recorded. The covariance in the parameters came from a Jacobian approximation to the Hessian of the least squares objective function, provided by the lmdif routine of the MINPACK library on which SCIPY.OPTIMIZE.LEASTSQ relies. The χ, η coordinate system is equivalent to the $\alpha\cos\delta$, δ coordinate system. If sigma clipping reduced the number of remaining observations below 10 then the source reverted to a mean position and error, as above.

2.4.3 Iterative re-matching

After initial source matching and fitting of astrometric solutions, subsequent source matching operations were performed slightly differently to those described in Section 2.4.1. Fig. 2 illustrates the process of SL refinement for a single source. The objective now was to take the complete but contaminated SL, refine the time series for all sources, and reduce the level of contamination. For coordinate

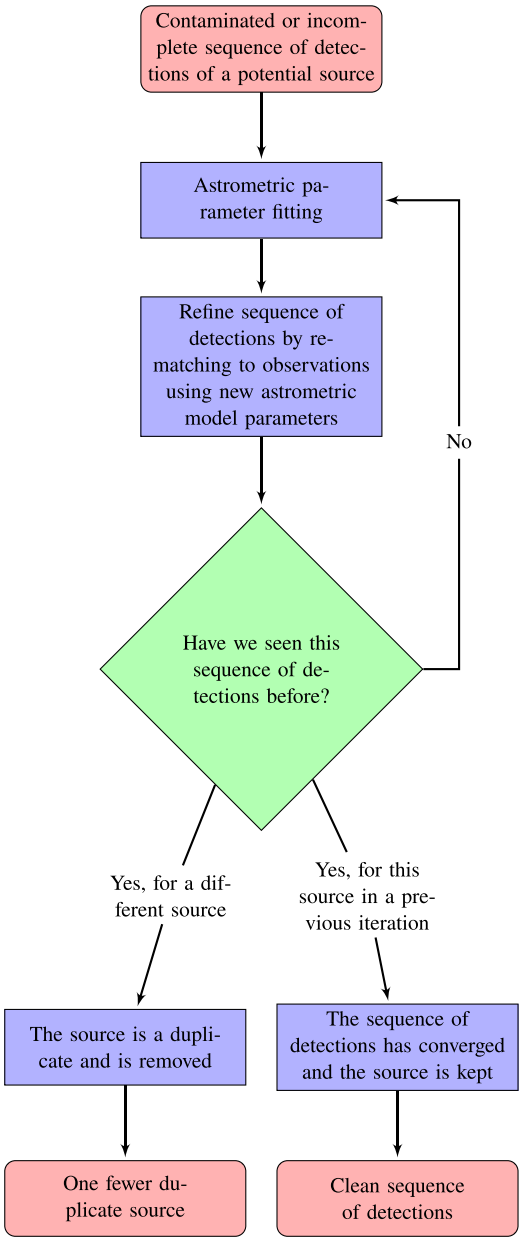

Figure 2. An illustration of the iterative process of refinement of the sequence of VISTA detections of a single source.

propagation we now used the internally determined best-fitting five-parameter astrometric solutions for sources with ≥ 10 detections, and mean field astrometry and average positions for sources with < 10 detections.

As in Section 2.4.1, we propagated the positions of sources to the epoch of each VISTA catalogue, but this time we simply found the closest VISTA catalogue match within our 0.339 arcsec and 5× error matching radius. This now meant that multiple SL entries could incorporate a single VISTA detection (which is a valid treatment of e.g. blended sources). This made identification of the majority of duplicates trivial, since they ultimately converged to the same set of VISTA catalogue detections.

We no longer appended unmatched VISTA catalogue rows to the SL, since our SL at this stage should be as complete as was practical. The sequence of VISTA catalogue detections (which in practice was a sequence of catalogue row indices) for each SL row was hashed (i.e. assigned a pseudo-unique reference integer for a given sequence, for ease of comparison and memory efficiency) and recorded. Duplicates of hashes therefore indicated duplicated sequences of detections and hence duplicated sources. Hashes were compared to all others in the SL and where they had been seen elsewhere the source was considered a duplicate and removed.

Finally, to determine whether a source had converged we looked for its current hashed list of VISTA catalogue indices among those from all of its previous iterations. If the current hash had been seen previously then the source was considered to have converged. Sources which had not yet converged had their astrometric solutions refitted as described in Section 2.4.2 and this re-matching procedure was then repeated until all sources had either been removed as duplicates or had converged.

As mentioned, sources with only a mean position and error used the mean proper motion of nearby sources and a parallax of zero for matching purposes. Once such a source converged we nullified its proper motion and parallax in the output catalogues.

2.4.4 Additional duplicate flagging

At the iterative re-matching stage obvious duplicates were removed by identifying identical lists of VISTA catalogue detections. This strict comparison could leave additional less obvious duplicate sources in the SL. It required a time series difference of only a single VISTA detection to pass the earlier method of checking, which was not uncommon with hundreds to thousands of observations (depending on sky location).

The remaining potential duplicated entries were found by identifying groups of sources within 0.339 arcsec. The source in this group with the most detections was considered the primary source, and all others were flagged as duplicates where they shared more than 20 per cent of their VISTA catalogue detections with other sources in the group. The 20 per cent threshold was necessary to accommodate situations in which a star with e.g. high proper motion happens to be blended with another at the reference epoch (2014.0) and hence was within the 0.339 arcsec threshold, yet was not a genuine duplicate. Such an occurrence is generally improbable for a given source, but among $\sim 10^9$ sources it does happen (see e.g. McGill et al. 2019). Approximately, 19 per cent of sources were flagged as probable duplicates.

2.4.5 Ambiguous match flagging

Our iterative matching routine (Section 2.4.3) allowed multiple sources to associate with single VISTA detections. We identified and flagged these cases in the time series data as ambiguous matches. For primary sources (i.e. those that are not probable duplicates), we flagged detections as ambiguous only where the detection was shared with another primary source. The number of ambiguous detections is provided in the catalogue for each source.

2.4.6 Observation counts

To determine whether a given source was likely to have been covered by a given observation we first propagated its equatorial position to the epoch of the observation. We then projected the propagated sky coordinates to VIRCAM array coordinates using the skycoord_to_pixel function of the Astropy WCS module using the

CASU WCS of the original image, and checked this position against a master confidence map.

Our master confidence map is an average of a random selection of confidence maps from late in the survey. We applied a minimum spatial filter, whereby each pixel was assigned the minimum confidence out of itself and its direct neighbour pixels. The application of the minimum spatial filter meant we were effectively requiring all nearby pixels to meet the threshold. This was also necessary to take into account imperfections in the master confidence map due to inherent variation in dither offsets between observations. We simply required a confidence level > 25 for a given position to be considered covered by a given observation. We used an average confidence map since heavily saturated sources can also produce regions of low confidence on single maps, and we did not want to erroneously reduce the observation counts of saturated stars. Without this consideration we would inflate their ratio of detections to observations, which we have found to be a useful indicator of the reliability of the data for each source (see Section 3.1).

There is inherent uncertainty in many stages of this procedure and it should therefore be stressed that the provided observation counts are approximate. To illustrate this, we note that 0.6 per cent of sources have more K_s band detections than the number of observations determined by this procedure. Since a source could only be assigned one detection per observation (though a detection could be assigned to multiple sources), this clearly indicates an error in the number of observations. The number of observations of each source is provided in the catalogue, alongside the number of detections.

2.5 Photometric calibration

The pipeline until this point was largely concerned with the production of a complete catalogue of sources with high-quality astrometry and a low level of contamination. This catalogue now allowed us to accurately calibrate the VISTA photometry. We performed this calibration in two stages. The first stage was a coarse survey-wide approach which aimed to anchor the instrumental photometry on to an absolute photometric reference frame. The second stage was a finer calibration at a subarray level that aimed to further reduce scatter in individual light curves.

We note that the photometric calibration component of the pipeline was produced using the VIRAC2β version of the catalogue. See Appendix A for details. The main differences between this preliminary version and the final catalogue version were restricted to astrometric enhancements and minor changes to the time series of individual stars. Considering this, and the considerable computational expense of the photometric calibration, we deemed it unnecessary to rerun this component with the final catalogue version.

Components of the photometric calibration strategy used varying criteria for selection of reference stars. Common source-specific criteria were

(i) sources have five-parameter astrometric solutions and are not flagged as possible duplicates;
(ii) sources have no detections that were ambiguously associated with another source;
(iii) sources were detected in at least 30 per cent of their K_s-band observations.

Common detection-specific criteria were

(iv) detections are 'perfect' according to DoPhot (i.e. flagged as well fitted by the PSF model);
(v) detections have $\chi < 5$ as measured by DoPhot;
(vi) detections have instrumental magnitude error < 0.5;
(vii) detections are not associated with multiple sources;
(viii) detections were not outliers at the 5σ level.

We also incorporated some more specific criteria which will be described in the relevant places, but we will refer back to this list as necessary.

We note that stars that exhibit significant variability represent a tiny fraction of the content of the catalogue, so their impact should be negligible. Even so, each component incorporated some form of outlier removal which should further reduce their impact.

2.5.1 *Primary calibration*

We used an SDSS ubercal (Padmanabhan et al. 2008) inspired approach, whereby spatial- and time-dependent magnitude offsets were fitted for such that they reduced the photometric residuals between successive observations of the same stars. This approach was ideally suited to the VISTA/VIRCAM observing strategy as there is a near guarantee of at least two observations of a given star on different parts of the focal plane, due to the VIRCAM pawprint pattern. Isolated reference stars which were also observed by the two-micron all sky survey (2MASS; Skrutskie et al. 2006) were used to anchor to the photometric system defined by González-Fernández et al. (2018) (see in particular their equations 5–9).

The functional form of our initial calibration from instrumental to VISTA magnitudes was

$$m_{\rm VISTA} = m + ZP + F(c,t) + I(xy),$$

where $m_{\rm VISTA}$ is the magnitude of a source in the VISTA system, presumed known for 2MASS reference sources and unknown otherwise. m is the instrumental magnitude of the source in a given detection and the calibration coefficients were as follows:

ZP - the overall zero point offset for the relevant bandpass.
$F(c,t)$ - an offset for each chip (c) in each observation (t).
$I(xy)$ - an offset dependent on position on the chip (xy) for a given chip. This is commonly referred to as the illumination correction map, and corrects the detector systematics shown in section 7.3 of González-Fernández et al. (2018). Each detector is subdivided into 128×128 spatial bins and we fitted for a magnitude offset in each bin. One $I(xy)$ map is measured per bandpass. We tested the use of bilinear interpolation for $I(xy)$, but found negligible improvement over simply using the nearest neighbour.

To solve for the calibration coefficients we used the L-BFGS-B minimization algorithm through the minimize function of the scipy.optimize module. The contribution to the objective function of a 2MASS reference source (i.e. a source with a presumed known $m_{\rm VISTA}$) with n (chronologically ordered) observations was as follows:

$$g = \sum_{i=1}^{n} \left(\frac{m_{\rm VISTA} - m_i - (ZP + F + I)_i}{\sqrt{\sigma^2_{m_{\rm VISTA}} + \sigma^2_{m_i}}} \right)^2 \tag{3}$$

and the contribution to the objective function for a non-2MASS reference source with n observations was

$$h = \sum_{i=1}^{n} \left(\frac{m_j - m_i - ((F+I)_i - (F+I)_{i-1})}{\sqrt{\sigma^2_{m_{i-1}} + \sigma^2_{m_i}}} \right)^2, \tag{4}$$

where

$$j = \begin{cases} N, & \text{if } i = 1. \\ i-1, & \text{otherwise.} \end{cases}$$

Table 1. Initial photometric calibration statistics. The number of coefficients, the total number of detections across all reference sources, the number of elements in the design matrix, and the number of sources which are ZP anchors.

Band	Coefficients	N	$\boldsymbol{X}$ Size	ZP Anchors
Z	343 025	7.32×10^8	2.51×10^{14}	1374
Y	344 241	8.00×10^8	2.75×10^{14}	1378
J	374 561	1.60×10^9	6.01×10^{14}	3005 274
H	356 193	1.24×10^9	4.41×10^{14}	3003 461
K_s	3051 649	2.53×10^{10}	7.71×10^{16}	3439 410

The overall objective function then was simply

$$f = \left(\sum g + \sum h\right) N^{-1}, \tag{5}$$

where N is the total number of detections across all reference sources.

A reference source pool was selected based on sources that met all of criteria i, ii, and iii, and that had two or more detections in the relevant bandpass that met criteria iv, v, and vi.

From within the reference source pool described above, we identified zero point anchors as those that had 2MASS counterparts that were within 0.5 arcsec with 'AAA' photometric quality flags. They also had to be fainter than 12 mag in all 2MASS bands to avoid saturation in the VISTA images, and must have no other VIRAC2β sources within 2 arcsec that might be unresolved in 2MASS. An additional requirement for 2MASS reference sources was placed on their Schlegel, Finkbeiner & Davis (1998) $E(B-V)$, the threshold of which depended on the bandpass being calibrated: < 0.1 for Z and Y, < 0.8 for J and H, and < 1.0 for K_s.

The statistics provided in Table 1 indicate the scale of the minimization problem. The design matrices were very large, but they were also extremely sparse. The majority of design matrix rows had only four non-zero elements out of $\approx 350\,000$ ($\approx 3000\,000$ in K_s), and hence the problem was amenable to sparse matrix techniques.

We ran the minimization over 30 iterations. Successive iterations had stricter relative error and absolute difference requirements of the reference sources and lower $\frac{\Delta f}{f}$ termination tolerance. The first iteration rejected $> 10\sigma$ and > 1.0 mag residuals and terminated the minimizer at $\frac{\Delta f}{f} \leq 10^{-5}$ and those limits decreased linearly to the last iteration which rejected $> 3\sigma$ and > 0.1 mag residuals and terminated the minimizer at $\frac{\Delta f}{f} \leq 10^{-6}$. This minimization routine was run twice. The first run used the mean $m_{\rm VISTA} - m_i$ for detections of 2MASS reference sources as the starting zero point offset and 0 for all remaining coefficients, and its purpose was to obtain an approximate illumination map. A second run was then performed using the output illumination map and zero point offsets from the first run as starting values. The starting value of $F(c,t)$ was $2.5 \log \frac{T_e}{T_{eb}}$ where T_e is the exposure time of the given observation and T_{eb} is the mode of the exposure time distribution of observations in the lower bulge in the relevant bandpass. The lower bulge region is significant as this is where the majority of zero point offset anchors were located due to the low extinction requirement of 2MASS reference sources. This normalization between exposure times was most necessary for the Z, Y, J, and H bands, where the default exposure time is different between the disc and bulge and the overlap between them in terms of numbers of reference sources is relatively small. In the K_s bandpass the modal exposure time is $4s$ for all fields so the second run was not so crucial, but we performed it anyway out of an abundance of caution.

Fig. 3 shows the resultant K_s-band $I(xy)$ map. The CASU web pages[2] describe some of the defects which are apparent in the map.

2.5.2 *Secondary calibration*

During inspection of the outcome of the primary calibration described in Section 2.5.1, it became clear there remained coherent time-varying structures in maps of the residuals (see Fig. 4). Removing this structure with further processing was desirable, since doing so would reduce scatter in the light curves.

Visual inspection of a few hundred maps of the residuals to the primary calibration indicated that the patterns, spatial scales, and amplitudes of the coherent structures varied significantly over short time-scales and among observations of the same field. In addition, the density of available high quality reference sources varied significantly between fields. Given these considerations we again decided to fit Chebyshev polynomials of varying degrees to the offset between source magnitudes in a given observation from their average magnitudes across all observations, in a similar manner to the astrometric calibration method detailed above (see Section 2.3). Essentially, we were building a time-dependent illumination map, $I(xy,t)$ to reuse the notation of the primary calibration. However, here it had a lower effective resolution as we had far fewer reference stars in a single observation, and the effective resolution varied between observations to account for the varying numbers and spatial distributions of reference stars.

We generated a reference star candidate pool from stars that met all of criteria i and iii. In addition they had to have two or more detections that met criteria v, vii, and viii, and that had > 100 reference sources for all coefficients of the initial photometric calibration and that were not at the edge of the illumination map. The primary calibration component benefitted from an abundance of reference stars, hence the selection criteria for the secondary component was less strict.

For each reference star candidate we adopted the median magnitude of detections meeting the detection-specific criteria listed above as the 'true' magnitude. The median is more robust to outliers than other measures, and outliers were still present in our data to some degree despite the data quality requirements described above.

For a given observation, we selected stars from the above pool by additionally imposing detection-specific criterion iv. This criterion tends to remove fainter detections, so incorporating it when computing the median magnitudes would have biased them bright. The various selection criteria listed above left us with a list of high quality detections of reliable reference sources, with robustly measured average magnitudes that were anchored to the VISTA photometric system.

The fit itself was performed using 5-fold cross-validation to robustly measure the residuals to the Chebyshev polynomial fits through a pre-determined sequence of 3, 5, 7, 10, 13, 17, 21, and 25 deg. We stopped the sequence when the mean cross-validated standardized residual either: increased, in which case we used the previous value; or decreased by less than 1 per cent or we reached the end of the sequence, in which case we used the current value. The purpose of this procedure was to fit for what are fairly complex residual maps but to also avoid overfitting our data. Once we had determined the optimal number of Chebyshev polynomial degrees

[2] http://casu.ast.cam.ac.uk/surveys-projects/vista/technical/known-issues

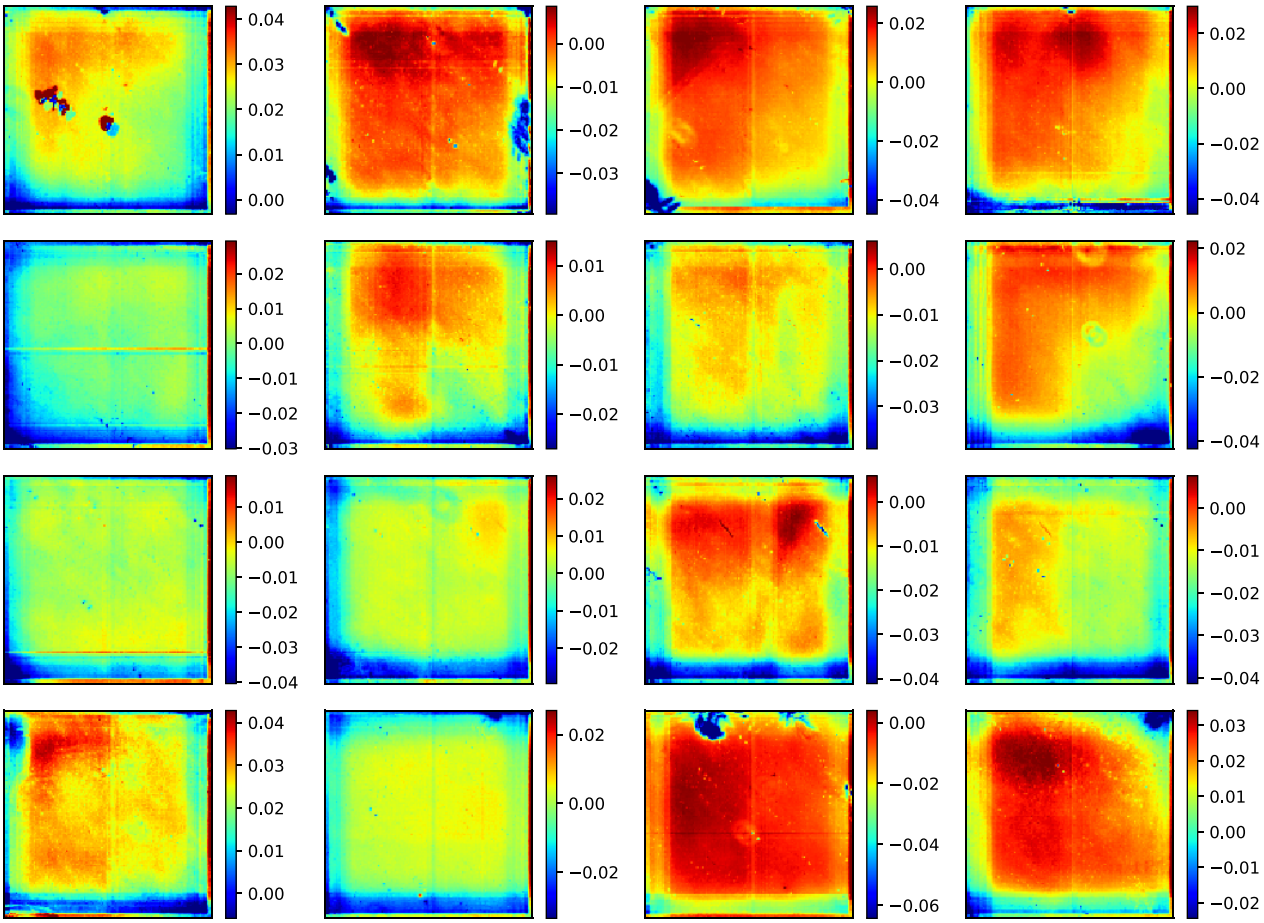

Figure 3. The fitted K_s-band $I(xy)$ illumination map. Detector numbers increase from left to right then top to bottom, e.g. the top left is detector 1, the top right is detector 4 and the bottom right is detector 16. Detector X-coordinates increase from left to right, and Y-coordinates increase from bottom to top. On the colour axis are the magnitude offsets, clipped at their 1st and 99th percentiles for clarity.

to achieve this balance we removed reference sources with cross-validated residuals greater than 3σ and refitted using all remaining reference sources. Application of the calibration was simply a matter of evaluating the fitted polynomials for every detection in each observation and subtracting the obtained offset. An example structure model is shown in Fig. 4.

Finally, to calibrate our uncertainties we adopted a similar method to that of the astrometric uncertainty calibration (see Section 2.3). For each detector in each observation we rescaled the DoPhot instrumental magnitude uncertainties by multiplying by a scaling factor and adding in quadrature a calibration uncertainty, as per equation (1). These values were acquired by minimizing the function below over N equal width magnitude bins:

$$\sum_{n=1}^{N}\left(\ln\left(k\cdot\mathrm{MAD}\left(\frac{m-\bar{m}}{\sigma_{\mathrm{VISTA}}}\right)\right)\right)^2 \tag{6}$$

where k is the 1.4826 approximate scaling factor to be applied to the MAD to obtain a reasonable estimate of the standard deviation that is robust against outliers; and $m-\bar{m}$ are the separations between the single epoch VISTA magnitudes and the median magnitudes across all selected observations. Rescaling the photometric uncertainties in this way served to bring the standardized residuals closer to unit Gaussian.

2.6 Photometry statistics

For individual detections we provide a photometric quality flag, to indicate where a detection has failed one or more criteria. These are supplied as integer values corresponding to six bit flags represented as an integer, and are as follows:

000001–1: no secondary photometric calibration applied,
000010–2: <5 secondary photometric reference stars per coefficient,
000100–4: in an edge bin of the illumination map,
001000–8: <100 reference stars for the primary calibration $I(xy)$ coefficient,
010000–16: <100 reference stars for the primary calibration $F(c,t)$ coefficient,
100000–32: <100 reference stars for the primary calibration ZP coefficient.

The photometric error flag supplied for a detection is the combination of its bit flags, i.e. the sum of the integer values listed above.

We provide some basic statistics for each bandpass to characterize the photometric time series of all sources. Statistics were computed using only high-quality observations. The requirements for a detection to be included in the photometric sequence for the purposes of computing statistics were

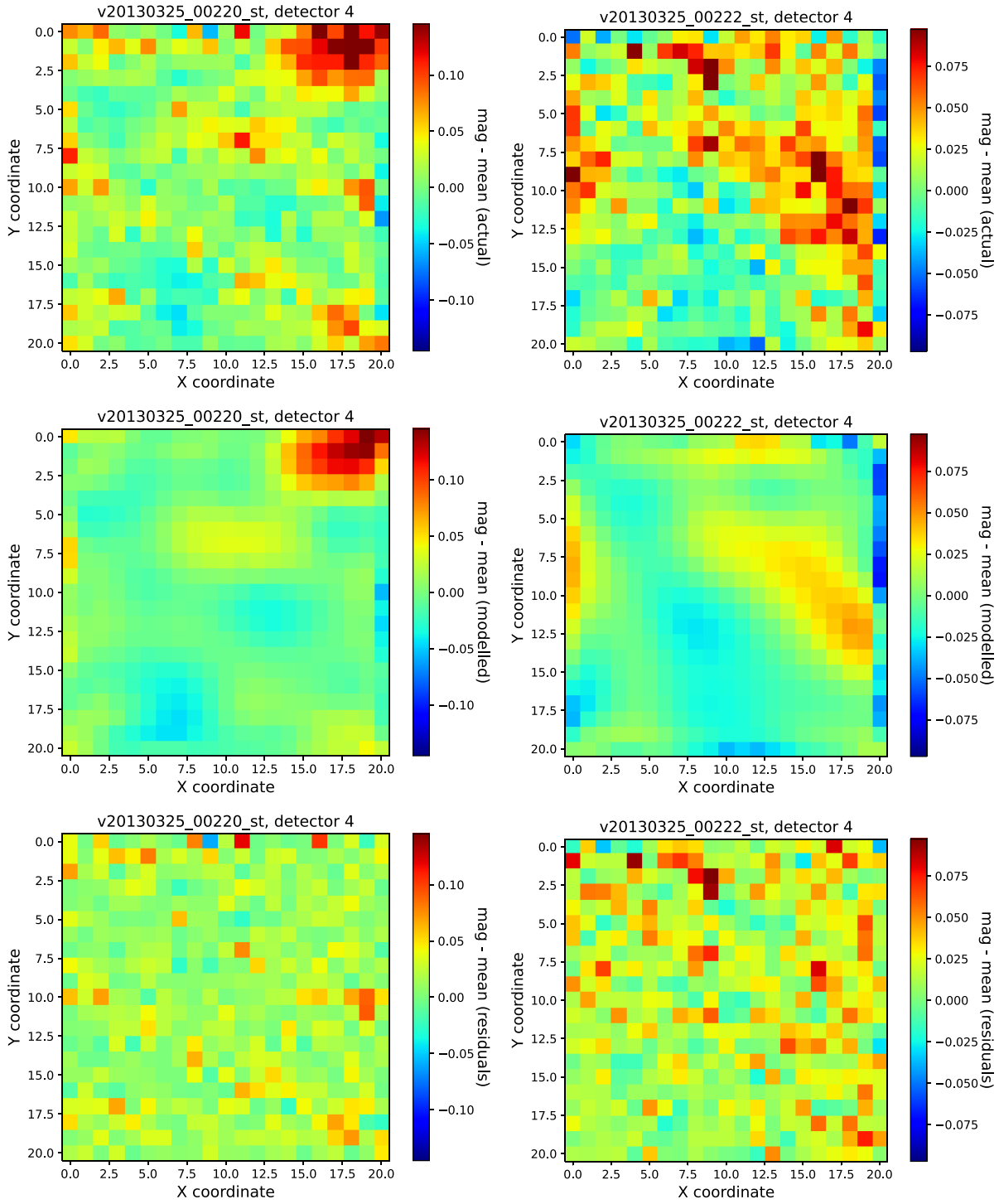

Figure 4. The left and right columns show results for detector 4 from two separate exposures, taken a few minutes apart and overlapping by half a detector. *Upper panels*: Binned magnitude offsets of stars between their time-series averaged magnitude and those of these example exposures after the primary photometric calibration has been applied. The structure indicates there is additional systematic signal to be cleaned from the photometry. The difference between the left and right exposures indicates that the systematic signal varies on short time-scales. *Middle panels*: Our fitted model of the offsets shown in the upper panels. *Lower panels*: Residuals remaining after subtraction of the fitted model signal from the input signal.

(i) zero photometric quality flag, i.e. it failed none of the criteria listed above,

(ii) not flagged as ambiguous (see Section 2.4.5), and

(iii) not an astrometric outlier above the 5σ level.

All three of these criteria had to be met. All detections, regardless of these quality criteria are included in the time series data sets, should one wish to recompute statistics with a different set of criteria. The number of detections that con-

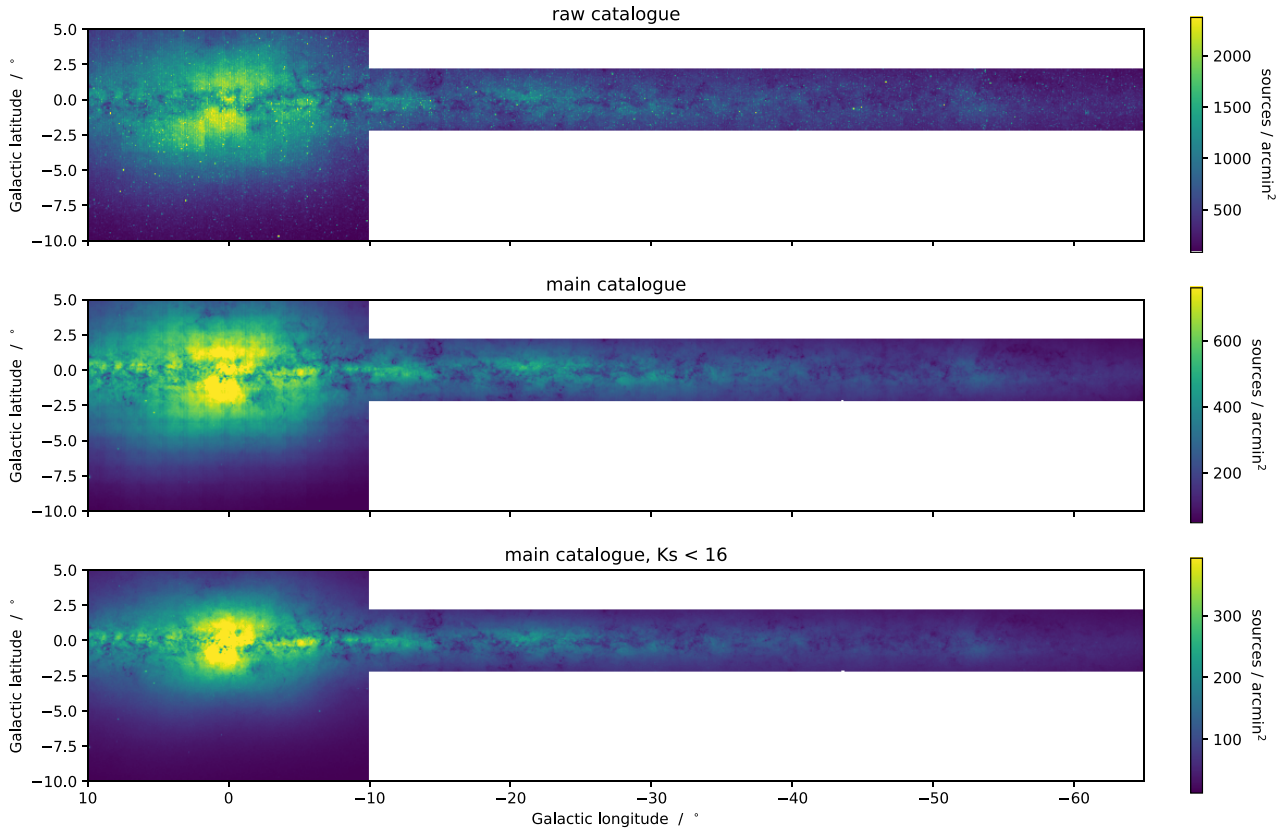

Figure 5. *Upper*: Density map of sources in the raw catalogue. Visible are apparent cluster-like high-density regions around bright sources caused by false detections in their wings. An additional lower level increased density due to DoPhot erroneously fitting sky noise as sources is also visible, particularly along the boundary of the high observing cadence region ($1.6 \lesssim l^\circ \lesssim 7.5$, $-3.6 \lesssim b^\circ \lesssim -1.5$). *Middle*: Density map of sources meeting the selection criteria used to define the main catalogue. The majority of the non-astrophysical inhomogeneity seen in the upper panel has been removed. What remains is largely due to varying detector sensitivity. *Lower*: Density map of sources meeting the selection criteria used to define the main catalogue that also have mean K_s band magnitude below 16, where completeness is universally high. This map is essentially free from survey-related density fluctuation.

tributed to the statistics in each bandpass is provided in the catalogue.

Note that the set of observations contributing to the photometric statistics differed from that used for fitting the mean astrometry. Firstly, for astrometric purposes the photometric quality flags were ignored. Secondly, the 5σ astrometric outlier cut was applied using the cross-validated residuals in the case of mean astrometry fitting, and using residuals to the output mean astrometry in the case of photometric statistics computation.

The photometric statistics provided are the mean magnitude and the standard deviation of the magnitudes in each bandpass. In addition, for the K_s bandpass only, we provide some additional statistics describing the photometric time series. These are: The modified Julian day of the first and last epochs; the skewness (corrected for statistical bias); a selection of percentiles – 0, 1, 2, 4, 5, 8, 16, 25, 32, 50, 68, 75, 84, 92, 95, 96, 98, 99, and 100; the MAD from the median; the median photometric uncertainty; the Stetson I, J, and K indices (Welch & Stetson 1993; Stetson 1996); and the von Neumann ratio η (von Neumann 1941, 1942). Note that when computing the Stetson indices we considered observations taken within 1 h to be contemporaneous, for the purpose of identifying observation pairs. The number of observation pairs that contributed to the Stetson I and J indices for each source is also provided. For the Stetson J index, we included unpaired observations with half weight.

3 THE CATALOGUES

The outcome of running the pipeline processes described in Section 2 was a raw catalogue of 1 390 256 078 tentative sources. The density of these on the sky is shown in the top panel of Fig. 5. Of these, 1 025 855 108 had five-parameter astrometric solutions, and 364 400 970 had two-parameter astrometric solutions (average positions). Of the rows with five- and two-parameter solutions, 23 per cent and 12 per cent were flagged as probable duplicates, respectively – 20 per cent of the raw catalogue in total.

3.1 Rejection of unreliable sources

The upper panel of Fig. 5 shows the source density of the raw catalogue and exhibits many survey-related, or other non-astrophysical features which should ideally be removed. Ground-based NIR observations tend to be relatively noisy compared to optical observations, and the configuration parameters we used for DoPhot caused it to occasionally report detection of sources that were simply image noise. In addition, the wings of bright stars also gave rise to many erroneous detections (see Fig. 1). Requiring multiple matched detections helped enormously with rejecting the erroneous ones, but with hundreds or thousands of coincident observations, false detections matched together by chance fairly frequently. This was particularly common where the false detections cluster together,

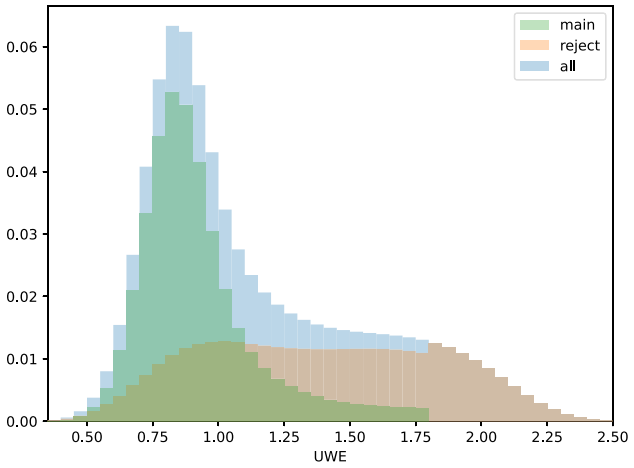

Figure 6. Distribution of the VIRAC2 UWE parameter for the raw catalogue (blue shaded), the main subset (green shaded), and the reject subset (orange shaded).

which happened most frequently in the wings of bright sources even though the VISTA/VIRCAM diffraction pattern is not constant for a given orientation. These were the main sources of contaminants in the raw catalogue.

In addition to rejecting probable duplicates (sources within 0.339 arcsec of another that share most of their detections), we employed two methods of identifying and rejecting probable contaminants from the raw catalogue. The first was a requirement that sources be detected in more than 20 per cent of the observations that cover them. It follows that the more observations there are, the more likely it is that erroneous detections will occur within the matching radius. This was particularly evident in the eight high-cadence tiles (covering $1.6 \lesssim l^\circ \lesssim 7.5$, $-3.6 \lesssim b^\circ \lesssim -1.5$), where there were a few times more observations than was typical for the other bulge fields. Due to overlapping VIRCAM pawprints, some small regions have a little over 2000 observations. A requirement of a > 20 per cent detection fraction, rather than a flat number of detections, acted to reduce and homogenize the contamination rate across the survey. The other major discriminator of contaminants was their astrometric goodness of fit. The residuals to the astrometric solutions of well-behaved sources are adequately characterized by their uncertainties, while this is typically not the case for the contaminants. Non-single stars have an additional component of motion that the five-parameter astrometric model does not account for, but this is highly unlikely to be significant in our data. The unit weight error (UWE) is defined as

$$\mathrm{UWE} = \sqrt{\frac{\chi^2}{N-M}}, \tag{7}$$

where χ^2 is the chi-squared statistic of the astrometric fit, the sum of the residuals squared divided by their uncertainties squared; N is the number of measurements, in our case one per dimension per observation; and M is the number of parameters solved for, in our case $M = 5$ (we computed goodness-of-fit statistics only for five astrometric parameter solutions). Sources whose residual scatter is well characterized by their uncertainties are expected to have UWE $\approx$ 1. In addition to the above selections, we employed a UWE < 1.8 cut, which rejected a further 3 per cent of the remaining sources.

Fig. 6 shows the distribution of UWE for the raw catalogue and our (eventual, see below) main and reject subsets. The jump in the reject distribution at UWE $= 1.8$ occurs due to the aforementioned rejection of stars at UWE > 1.8. The peak of the distribution occurs at UWE ≈ 0.85, where it should ideally occur at UWE ≈ 1.0. We speculate that this might be due to an overestimation of the VISTA per-epoch positional uncertainties (see Section 2.3). It is well established the *Gaia* uncertainties tend to be underestimated (see discussion in Section 3.2.1). These come into play through equation (2), as σ^2_{Gaia}, whereby an underestimate would cause $\sigma^2_{\mathrm{VISTA}}$ to be overestimated. We are ultimately not concerned by the potential overestimation since the uncertainties on the mean astrometric parameters appear to be fairly reliable (see Section 3.2.1).

Since the minimum number of observations covering any region of the survey was ≈ 50, and a five astrometric parameter solution is a de-facto 10 epoch requirement, the 20 per cent detection fraction requirement is a de-facto five astrometric parameter solution requirement. In addition, we did not compute any goodness-of-fit statistics for two parameter astrometric solutions, meaning the UWE discriminator was unavailable for these sources. For these reasons, we elected to explicitly impose the five astrometric parameter solution requirement.

On application of the five astrometric parameter, non-duplicate, greater than 20 per cent detection fraction, and UWE < 1.8 selection we were left with a catalogue containing 545 346 537 sources, that was largely free from contamination. This is the main component of the VIRAC2 astrometric catalogue. The density map of this selection is shown in the middle panel of Fig. 5. We can now begin to pick out by eye some of the larger Galactic globular clusters that were previously hidden among the false detections – NGCs 6440, 6544, 6553, 6626, 6656, and 6441 are all visible in the bulge on close inspection. The principal remaining source of non-astrophysical inhomogeneity is visible as a grid-like pattern across the survey and is due to varying detector sensitivity. If one wishes to remove this, and obtain a selection with a largely uniform high completeness and relatively low contamination then a further selection of $\mathrm{K_s} < 16$ mag will achieve this. Using artificial source injection, Sanders et al. (2022a) determined that this selection is at least 90 per cent complete everywhere except the few square degrees around the Galactic Centre (see their appendix C). This selection is demonstrated in the density map shown in the lower panel of Fig. 5, and is seen to be essentially free of non-astrophysical inhomogeneity.

We note that the 20 per cent detection fraction is the main cause of rejection of genuine sources. Stars at the faint end of the survey naturally tend not to be reliably detected, causing them to fail this selection where they might not necessarily fail the others. Transient stars also can suffer from rejection as a result of this criterion. In a survey of the $\Delta K_s > 4$ mag stars by Lucas et al. (2024), which did not apply this criterion, approximately 10 per cent do not meet the detection fraction threshold. These tended to be novae and other short-time-scale transients. The principal aim of this work was the production of a highly reliable astrometric catalogue, and our selection criteria were set to achieve this. However, we recognize that much useful data remains among the sources that we have rejected, and hence we publish the VIRAC2 reject catalogue alongside the main VIRAC2 catalogue.

3.2 Astrometric precision

Fig. 7 shows the distribution of the uncertainties on proper motion in right ascension and parallax as a function of K_s band mean magnitude for the main catalogue. Peak astrometric performance is in the $11 < K_s$ mag < 14 range, where proper motion uncertainties are typically better than 0.5 mas yr^{-1} per dimension (median 0.36

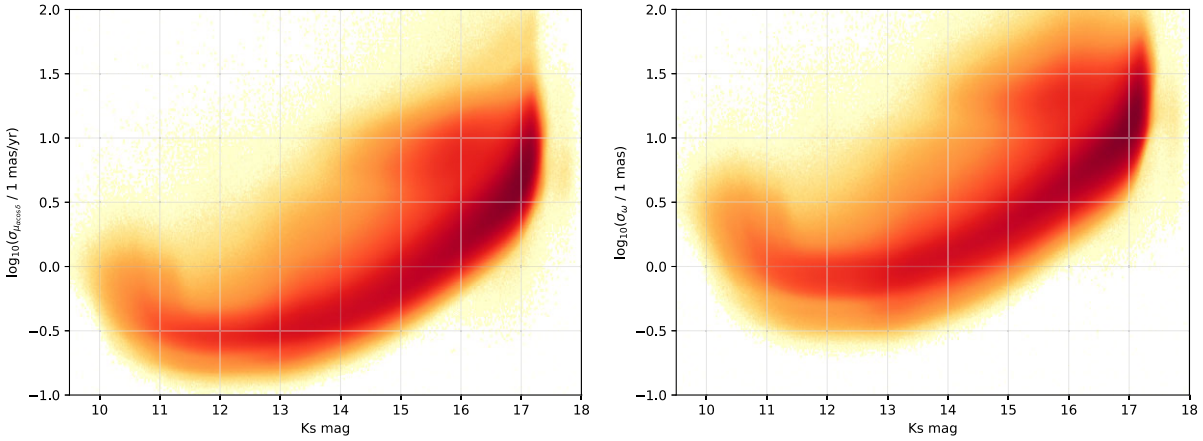

Figure 7. *Left*: Uncertainty in $\mu_{\alpha\cos\delta}$ versus K_s band mean magnitude for the main catalogue. *Right*: Parallax uncertainty versus K_s band mean magnitude for the main catalogue. For both plots the colour axis is logarithmic.

and 0.38 mas yr^{-1} for $\mu_{\alpha\cos\delta}$ and μ_δ, respectively) and parallax uncertainties are typically around 1 mas (median 1.02 mas). Saturation impacts performance for stars brighter than this. Performance at $K_s = 16$ is typically around 1.5 mas yr^{-1} per dimension for proper motion and 5 mas for parallax. The faint cloud visible above the main locus in the $15 < K_s$ mag < 16.5 range ($\sigma_{\mu_{\alpha\cos\delta}} > 5$ mas yr^{-1}, $\sigma_\omega > 10$ mas) is primarily comprised of false sources that still pass our UWE < 1.8 cut. Application of a more strict selection (e.g. UWE < 1.4) will generally remove them if a more robust sample is required, at the cost of some genuine sources.

3.2.1 *Validation with Gaia DR3*

We performed a 0.25 arcsec nearest neighbour cross-match of the VIRAC2 main catalogue to Gaia DR3, finding that 233 235 552 VIRAC2 sources (43 per cent) have *Gaia* counterparts, of which 176 954 558 (32 per cent of VIRAC2 sources) have 5 or 6 parameter mean astrometry in the *Gaia* catalogue.

This sample will be broadly similar to the selection of reference stars used for the initial astrometric calibration (see Section 2.3). For these, we should expect the VIRAC2 mean astrometry to match fairly closely that of *Gaia* DR3. Fig. 8 shows the 1D histograms of standardized offsets (i.e. offset divided by its error) in parallax and the two components of proper motion for this sample. If the uncertainties on the offsets are truly 1σ Gaussian, then we should find that the histograms match the probability distribution function of a unit Gaussian. In fact we find that the parallax distribution resembles a Gaussian distribution with $\sigma = 1.1$, and the distributions of the two components of proper motion resemble a Gaussian distribution with $\sigma = 1.2$. This modest difference implies that the uncertainty on the offsets is underestimated by approximately 10 and 20 per cent in parallax and proper motion, respectively.

The simplest explanation for an underestimate in the uncertainty on the offsets is that the uncertainties on the parameters themselves are underestimated. Through experimentation we found that in order for each distribution to resemble a unit Gaussian we had to either inflate Gaia uncertainties of all three parameters by a factor of approximately 2.25; or inflate VIRAC2 proper motion uncertainties by a factor of approximately 1.25 and parallax uncertainties by a factor of approximately 1.1. In practice, scaling factors should be applied to the per-epoch astrometric uncertainties and propagated through to the mean astrometry parameters. There is evidence presented in

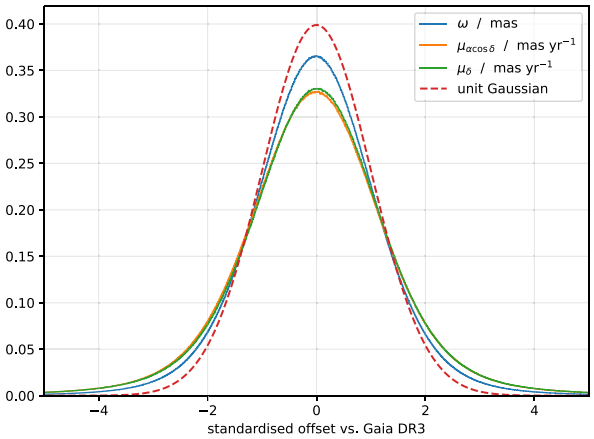

Figure 8. Standardized offsets between VIRAC2 and *Gaia* DR3 mean parallax and proper motion components. A unit Gaussian probability distribution function is shown for comparison. Gaussian distributions with $\sigma = 1.1$ and $\sigma = 1.2$ match closely the parallax and proper motion histograms, respectively. This implies that the uncertainties on the offsets are underestimated by approximately 10 per cent for parallax, and 20 per cent for proper motion, but caution should be used when interpreting this figure. See the text for a more thorough analysis.

Section 3.1 that potentially supports the conclusion that the VISTA per-epoch uncertainties are mild overestimates, namely that the unit weight error distribution peaks slightly below 1.0. Further testing might enable us to apportion blame, though these data are not yet public for *Gaia*. El-Badry, Rix & Heintz (2021) and Sanders (2023) find that *Gaia* DR3 parallax uncertainties are underestimated by up to a factor of 2, particularly for red sources (which are the dominant component of our sample) and those with RUWE > 1.4 (see their section 5). Refinement of the sample selection to have both *Gaia* DR3 RUWE < 1.4 and VIRAC2 UWE < 1.4 yields only a modest improvement, to around $\sigma = 1.05$ and $\sigma = 1.15$ for parallax and proper motion, respectively. This indicates that underestimated uncertainties, if present, are a more general problem not restricted only to the subset of poorly measured sources.

A common practice in least squares fitting is to scale the covariance matrix such that the reduced chi-squared equals unity. This is typically necessary when it is known that the uncertainties on the

data points are unreliable, as was the case for VIRAC2β (see Appendix A). For the main pipeline run we considered the centroid errors to be significantly more reliable, and hence the rescaling to be unnecessary. The peak of the distribution of the unit weight error being reasonably near unity indicates that there was indeed limited need. However, should users wish to apply this correction then they should simply multiply the individual parameter uncertainties by the unit weight error. We note that as the posterior probability density functions are relatively simple in this case, rescaling the parameter errors in this way approximates parameter uncertainties produced by Markov chain Monte Carlo methods that incorporate an error scaling factor.

Another explanation could be mismatches between VIRAC2 and *Gaia* DR3 sources. Cross-matches between catalogues with large bandwidth and resolution differences are never perfect. In principle we could significantly reduce the 0.25 arcsec matching radius used. Typically VIRAC2 positional uncertainties are at the level of a few milliarcsec, and *Gaia* DR3 is similar for the faintest sources and much better for brighter ones. However, in doing so we would bias the selection towards only those with agreement in mean astrometry, thereby invalidating this comparison.

We must also consider that this sample is only broadly similar to that used for the initial astrometric calibration. We did not impose any goodness-of-fit statistic requirements on the *Gaia* sources this time, nor was every VISTA detection that was used for astrometric calibration also used for mean astrometric parameter fitting. Technically, we were comparing mean astrometric parameters at epoch 2014.0 for VIRAC2 and epoch 2016.0 for *Gaia* DR3, though this should have a negligible impact in practice.

It is important to note that a modest underestimate in the errors on the offsets is unlikely to have only a single cause. Additionally, there are reasons to suspect that the offsets might be biased towards larger values. Given this, and that the apparent underestimates are relatively minor, we consider that the VIRAC2 catalogue mean astrometry and their uncertainties are valid.

3.2.2 *External validation with HST*

Luna et al. (2023) compared *Hubble Space Telescope* (*HST*) proper motions from three crowded fields in the Galactic bulge to those of VIRAC2. They measured the multiplicative factor by which VIRAC2 proper motion uncertainties must be inflated to account for the scatter observed in their offsets from the *HST* measurements as a function of J-band magnitude. They found that a multiplicative factor of between 1.0 and 1.5, the larger value being necessary at brighter J-band magnitudes and in the densest field tested, but a value near unity was broadly correct. Ultimately, they concluded that no inflation factor was necessary, potentially further indication that it is the *Gaia* uncertainties that are underestimates.

3.2.3 *Known failure modes*

In the special case of large amplitude variable sources in crowded fields, the astrometric solution could become unreliable due to systematic changes in the location of the centroid found by DoPhot. This could occur if stars adjacent to the variable star were no longer detected when the latter became much brighter. This issue was noted by Lucas et al. (2024), in the context of highly variable giant stars in the nuclear disc of the Milky Way. Some additional failure modes that were identified during nearby object searches are detailed in Appendix B.

Population studies can be performed with relative confidence, but we caution the reader that attempts to select outliers (e.g. high proper motion or parallax sources) will tend to also preferentially select the erroneous examples. Care must be exercised in cleaning such samples.

3.3 Time series data

Photometric time series are supplied alongside their aggregated stats. Astrometric time series are also supplied, as both calibrated equatorial and array coordinates. The schema of the time series table is provided in Table C2.

We have found that erroneous photometric outliers are typically evident through inspection of the *chi* and *ast_res_chisq* statistics, and whether or not the detection is flagged as an ambiguous match. Where *chi* was output directly from DOPHOT, *ast_res_chisq* is the χ^2 of the astrometric residual (with 2 degrees of freedom), and the ambiguous match flag was set to '1' if that detection also appears in the time series of another source (e.g. through blending).

A set of example K_s-band photometric time series for a range of brightness is presented in Fig. 9. The sources shown were selected from a pool of those with typical photometric uncertainties for their average magnitude. From this plot, it is evident that *ast_res_chisq* can be a useful statistic for rejection of erroneous data points.

3.4 Colour–magnitude diagram improvement

To demonstrate the improvements in the photometry and depth of VIRAC2 versus VIRAC v1, we provide colour–magnitude diagrams from both catalogues for the Galactic globular cluster Messier 22 (NGC 6656; see Fig. 10). All selected stars are within 0.2 degrees of the cluster centre. For VIRAC2, we included only stars in the main table (i.e. we did not include the *reject* table), and for VIRAC v1 we only included stars flagged as reliable. The VIRAC v1 selection comprises 17 075 sources, while the VIRAC2 selection comprises 100 657 sources. The extra ≈ 1 mag of depth is evident, as is a general tightening up of the various stellar sequences. We note that while VIRAC v1 tends to be better for saturated stars, these are often flagged as 'unreliable' and hence were not included in Fig. 10.

We direct those interested in CMDs in these regions to Alonso-García et al. (2018), whose catalogue is available from the VISTA Science Archive (VSA). The Alonso-García et al. (2018) catalogue required detections in three bandpasses, where VIRAC2 relies on astrometric goodness of fit and detection fraction to discern reliable sources from false. This means that sources which are non-detections in one or two bands, and hence are missing from the Alonso-García et al. (2018) catalogue, may be present in VIRAC2.

3.5 Catalogue description and access

The complete catalogues are available from the ESO archive at https://archive.eso.org. The table identifiers are as follows:

(i) VVVX_VIRAC_V2_SOURCES,
(ii) VVVX_VIRAC_V2_REJECTED_SOURCES,
(iii) VVVX_VIRAC_V2_LC,
(iv) VVVX_VIRAC_V2_REJECTED_LC, and
(v) VVVX_VIRAC_V2_OBS.

Where tables (i) and (ii) are the aggregate source data (e.g. positions, proper motions, and mean photometry), tables (iii) and (iv) are the time series data, and table (v) contains observation related

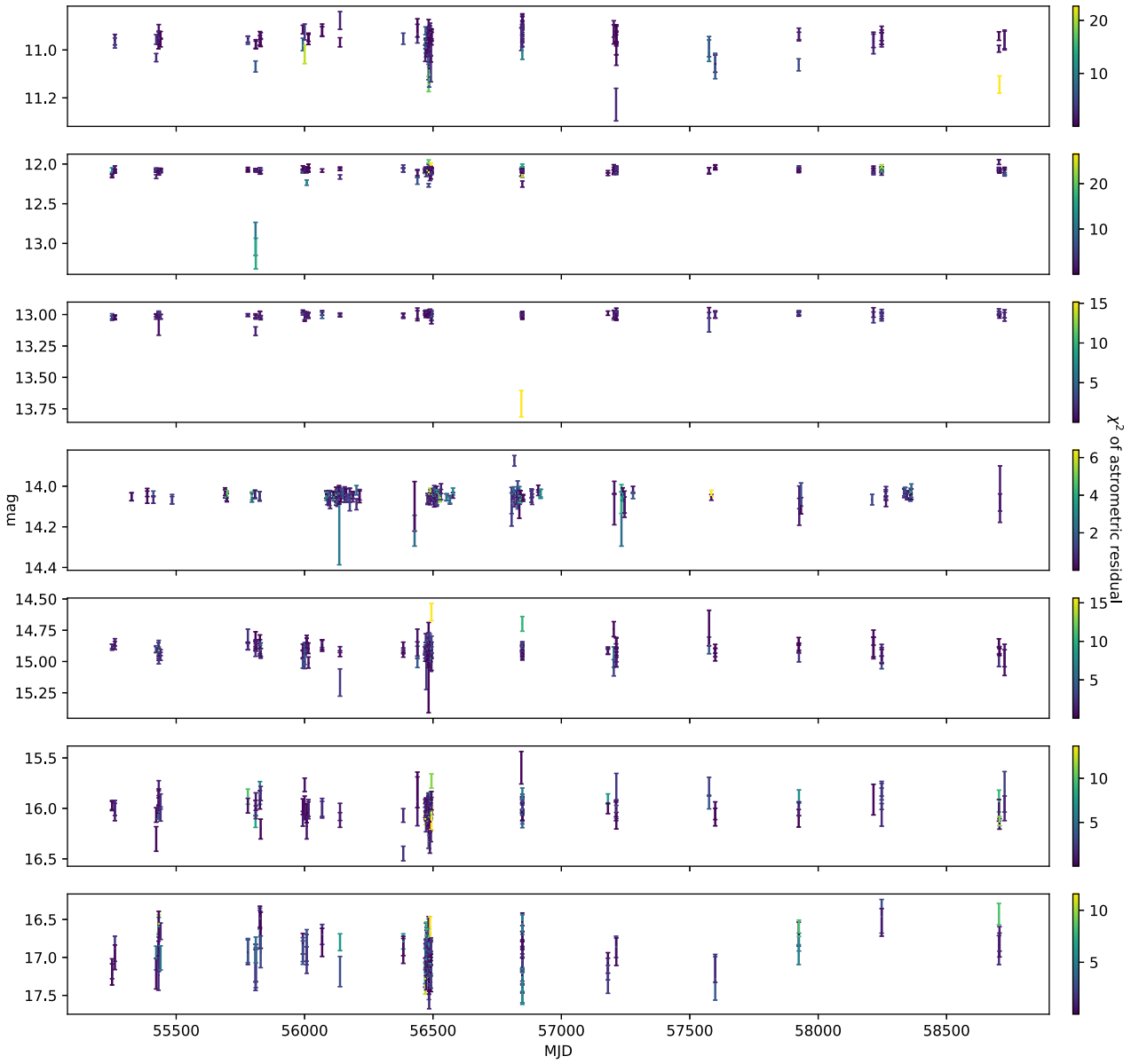

Figure 9. Example K_s band light curves at each integer magnitudes 11 through 17 in the K_s bandpass. Examples were selected from sources with $> 100 K_s$ band epochs, within 0.1 mag of the target magnitude, and with average K_s mag uncertainty within 5 mmag of what is typical for that magnitude. The colour axis shows the χ^2 (with 2 degrees of freedom) of the astrometric residual for each data point. It can be seen that outliers in magnitude space are often also outliers in the astrometry, making this a useful method for cleaning the photometric time series.

information (e.g. seeing and airmass). Tables (i) and (iii) are the main selection, and tables (ii) and (iv) are the reject selection.

Section 3.1 describes the make-up of the main and reject selections. Schemata and example rows for the source and time series tables are given in Appendix C.

The catalogues can be efficiently queried using the Table Access Protocol (TAP) via the ESO programmatic access tool,[3] or e.g. TOPCAT[4] (Taylor 2005). More information, including example queries, can be found in the document accompanying the ESO release.

[3] archive.eso.org/programmatic
[4] star.bris.ac.uk/ mbt/topcat

4 EXAMPLE APPLICATIONS

4.1 New stars and ultracool dwarfs in the solar neighbourhood

VIRAC2 parallaxes and proper motions can be used to discover new nearby stars and brown dwarfs in a similar manner to VIRAC v1 (Smith et al. 2018). This complements the Gaia Catalogue of Nearby Stars (GCNS; Reylé et al. 2021; Smart et al. 2021) and the earlier Gaia-based ultracool dwarf (UCD) search of Reylé (2018) by providing slightly better sensitivity to L and T dwarfs, which are optically very faint. While most VIRAC2-selected nearby sources are already catalogued in GCNS or earlier studies (see e.g. Mejías et al. 2022), we see below that the majority of VIRAC2 UCD candidates with visually confirmed high proper motions are new discoveries.

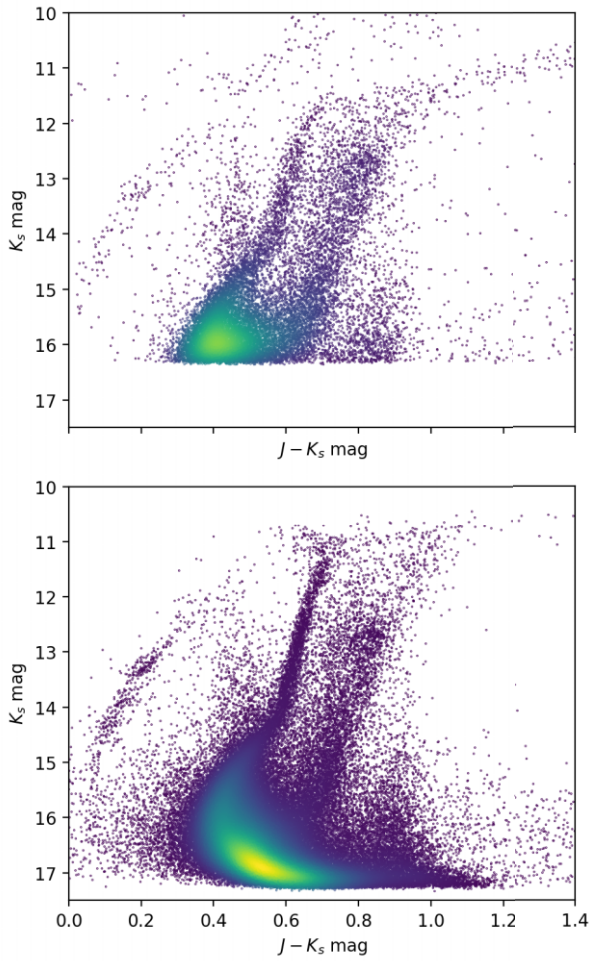

Figure 10. The $J - K_s$ versus K_s colour–magnitude diagram for the Galactic globular cluster NGC 6656 from VIRAC v1 (upper panel) and VIRAC2 (lower panel). The colour axis represents the density of points within the diagram (blue are isolated; yellow are highly grouped).

We searched for new UCDs and any other nearby sources that might have been missed by *Gaia* using the following initial selection in the VIRAC2 main source table:

(i) $\varpi > 10$ mas
(ii) $\varpi/\sigma_\varpi \geq 5$
(iii) $ks\_n\_det > 0.5 \times ks\_n\_obs$

where ϖ is the parallax and *ks_n_det* and *ks_n_obs* are the VIRAC2 parameters corresponding to the number of K_s detections of a source and the approximate number of K_s observations of the source's position, respectively.

Applying these four selection criteria returned 1576 427 sources from the data base, the great majority of which clearly had incorrect parallaxes. For example, the GCNS contains only 331 312 sources at distances $d < 100$ pc across the whole sky in the Gaia Data Release 3, so VIRAC2 should find far fewer in a survey of ≈ 1.4 per cent of the sky. Distinguishing bona fide nearby VIRAC2 sources from false positives is a difficult task, perhaps best suited to machine learning methods at this scale (Smart et al. 2021). Here, we focus mainly on UCDs, rather than attempting to recover all nearby stars, but colour blind searches for very high proper motion stars and stars within 50 pc of the sun were also attempted. To note, the candidate nearby stars selected above are widely distributed across the survey area but there is some degree of clustering in the fields with the largest number of observations, e.g. the Galactic centre tile and a group of eight contiguous VVV bulge tiles at $1.6 \lesssim l^\circ \lesssim 7.5$, $-3.6 \lesssim b^\circ \lesssim -1.5$. These fields all have a high source density.

4.1.1 *High proper motion search*

From the initial selection above, we selected sources with proper motion, $\mu > 500$ mas yr^{-1}, where μ is computed from the sum in quadrature of the two components of the proper motion. This yielded 20 889 candidates, most of which have a significant fraction of ambiguous detections in the time series. In fact, the spatial distribution of the 20 889 candidates shows a very strong clustering in the area of the eight contiguous high cadence tiles mentioned above, almost all of which are sources for which a large fraction of the detections are listed as ambiguous. Specifically, $f_{amb} > 0.9$, where f_{amb} is the ratio of VIRAC2 parameters *ks_n_amb*/*ks_n_det* and *ks_n_amb* is the number of detections with an ambiguous match to more than one VIRAC2 source, i.e. it is the fraction of ambiguous detections.

We applied the following three cuts to reduce the 20 889 candidates to a small number for visible inspection:

(i) $f_{amb} < 0.4$
(ii) $\Delta t > 0.5$ yr
(iii) $ks\_n\_det > 20$

where Δt is the time span defined by the VIRAC2 parameters *ks_first_epoch* and *ks_last_epoch*, the first and last modified Julian dates of the K_s detections in the photometric time series set (see Section 2.6). Bona fide high proper motion stars should pass these cuts since they would typically be expected to have only a small proportion of ambiguous detections, e.g. due to blending as the rapidly moving source passes close to another source in the field. They would also be expected to be detected over a time baseline of several years and to have a large number of detections. These cuts yielded a list of 21 candidates, 18 of which were confirmed as genuine high proper motion stars by visual inspection of a pair of images taken several years apart. The three false candidates were due in two cases to blended pairs of stars. In the third case, all the detections in the VIRAC2 time series were in 2010, save for a single detection in 2018 that appears likely to be noise, from inspection of the image.

The distribution of f_{amb} for candidates satisfying all the cuts except the one on f_{amb} is bimodal, with a very large number of false positives found near $f_{amb} = 1$ and genuine high proper motion stars making up a smaller peak near $f_{amb} = 0$. The cut at $f_{amb} = 0.4$ was chosen to exclude the larger peak of false positive sources. Since only two genuine sources were found with $0.2 < f_{amb} < 0.4$, we expect that relatively few sources with larger values of this parameter have been missed. However, this search did miss the T5 brown dwarf VVV J165507.13-421755.8 (Schapera et al. 2022), for which $f_{amb} = 0.78$, $\mu \approx 705$ mas yr^{-1} and $\varpi \approx 66$ mas ($d \approx 15$ pc). Its motion was detected via a machine learning analysis (Caselden et al. 2020) of the unWISE coadds (Meisner, Lang & Schlegel 2018) before then turning to VVV and VIRAC2 for clearer images and astrometry. Due to its large proper motion the VIRAC2 time baseline is short, $\Delta t = 3.9$ yr, because the source is blended with more than one star over the course of the VVV time series. This highlights the value of combining independent data sets for more complete searches.

The 18 genuine high proper motion sources include one new discovery, VVV J181453.17-265453.6, and 17 stars that are already

Table 2. Data for the brown dwarf VVV J1814-2654, discovered by the high proper motion search. The VIRAC2 J2000 coordinates are at epoch 2014.0. The absolute magnitude, M_{K_s}, is the median value and its error bars represent the 68 per cent confidence interval, after sampling over Gaussian distributions in ϖ and K_s with the quoted parameters to produce a probability distribution. The quoted K_s magnitude is the median value, given as the ks_p50 parameter in Table C1.

VIRAC2 source ID	13 333 546 009 625
Name	VVV J1814-2654
RA (hms)	18 14 53.17
Dec (dms)	−26 54 53.6
RA (°)	273.721554
Dec (°)	−26.914877
l (°)	4.965352
b (°)	−4.610297
$\mu_{\alpha\cos\delta}$(mas yr^{-1})	-235.1 ± 2.1
μ_δ(mas yr^{-1})	-446.7 ± 2.2
ϖ (mas)	36.4 ± 4.2
d (pc)	$27.1^{+3.6}_{-2.9}$
Z	>19.5
Y	18.49 ± 0.20
J	17.28 ± 0.12
H	16.35 ± 0.09
K_s	15.80 ± 0.10
M_{K_s}	$13.60^{+0.26}_{-0.28}$
$Z-J$	>2.2
$Y-J$	1.21 ± 0.23
$J-H$	0.93 ± 0.15
$H-K_s$	0.55 ± 0.13
$J-K_s$	1.48 ± 0.16
$z-J$	2.54 ± 0.28

in the GCNS and earlier lists of higher proper motion sources (Terzan et al. 1980; Lépine 2005, 2008; Beamín et al. 2013; Ivanov et al. 2013; Luhman 2014; Luhman & Sheppard 2014; Schneider et al. 2016; Klüter et al. 2018; Reylé 2018; Smith et al. 2018; Gentile Fusillo et al. 2021). Data for the new source, hereafter VVV J1814-2654, are given in Table 2. A finder chart is provided in Appendix D.

Nearby stars have negligible interstellar reddening so the non-detection in the VISTA Z passband, along with red $Y-J$, $J-H$ and $H-K_s$ colours, indicate that this is an UCD with a spectral type in the range L0 to T2 (see e.g. Kirkpatrick et al. 2021). The absolute K_s magnitude, M_{K_s} suggests a spectral type between T1 and T3, according to the data in Dupuy & Liu (2012). VVV J1814-2654 is therefore an early T dwarf candidate, though there is sufficient scatter in the M_{K_s} versus spectral type relation that a late L dwarf type is also quite possible. A cross-match to the Dark Energy Camera Plane Survey (DECaPS; Schlafly et al. 2018; Saydjari et al. 2023, see Section 4.1.3) provides an optical z-band detection and we note that the colour $z-J = 2.54 \pm 0.28$ is relatively blue for a T dwarf (see Section 4.1.4). However, the uncertainty is large and the data are consistent with a source near the L/T transition. We can therefore be confident that VVV J1814-2654 is a brown dwarf. The system is projected in the direction of the inner Galactic bulge, within 5° of the Galactic Centre in both longitude and latitude (see Table 2). Only two confirmed brown dwarfs: VVV BD001 and LTT 7251B (Beamín et al. 2013; Smith et al. 2018) have previously been found in the inner bulge, where the high stellar density (especially in the infrared) makes searches for high proper motion stars difficult. Given the current community effort to achieve a complete census of nearby stars and brown dwarfs (see e.g. Smart et al. 2021; Kirkpatrick et al. 2024), the discovery of VVV J1814-2654 at $d \approx 27$ pc, is a helpful addition. Such systems also make good targets for adaptive optics imaging to search for companions, given the abundance of suitably bright reference stars.

A high proper motion source was detected at the same location in VIRAC v1 (Smith et al. 2018) but the proper motion was smaller and quite different ($\mu_{\alpha\cos\delta} = -83.6$ mas yr^{-1}, $\mu_\delta = -171.1$ mas yr^{-1}) and no parallax value was reported, owing to the 5σ parallax threshold adopted in that work. Here, we have visually confirmed the motion, which was not done in Smith et al. (2018) for this source. The erroneous motion in VIRAC v1 was probably due to the effect of blending with an adjacent star of similar brightness and the use of aperture photometry. There is no detection in the Galactic surveys by the *Spitzer Space Telescope* (Werner et al. 2004, see further discussion in Section 4.1.3).

4.1.2 T dwarf search

T dwarfs with spectral types later than T0 typically have fainter M_{K_s} values and bluer $(J-K_s)$ and $(J-H)$ colours than brown dwarfs of earlier types. To search for T dwarfs, we began with the ∼1.6 million candidate nearby VIRAC2 sources with 5σ parallax detections selected in Section 4.1.

We then applied the following initial cuts:

(i) $M_{K_s} > 12$
(ii) $Y-J > 0.8$
(iii) $J-K_s < 0.9$
(iv) $Z-J > 2$ or no Z-detection.
(v) $\mu > 30$ mas yr^{-1}
(vi) $\Delta t > 3$ yr
(vii) $f_{amb} < 0.4$
(viii) $ks\_n\_det > 20$

The absolute magnitude and colour cuts were defined mainly from inspection of the data in Dupuy & Liu (2012) and Kirkpatrick et al. (2021), respectively. The L/T transition actually occurs at $M_{K_s} \approx 13$ rather than $M_{K_s} = 12$ but we adopted a 1 mag brighter threshold in order to include equal mass binary systems and allow for the significant scatter that exists in the spectral type versus absolute magnitude relation. The $Z-J$ constraint was also relaxed since the colour versus type relation is not well defined in the literature for the VISTA Z filter but we can be confident that T dwarfs will comfortably pass the $Z-J > 2$ threshold in the Vega system (see e.g. Hewett et al. 2006, for a very similar Z filter). The proper motion cut helps to remove false positives among the 1.6 million candidate nearby VIRAC2 sources that are actually distant stars. After applying these cuts, there were 750 candidates in the data base.[5]

Two additional parameters can be used to identify the best candidates for visual inspection: (i) the unit weight error (UWE) of the five parameter astrometric fit and (ii) $V_{\rm tan}$, the tangential velocity of the source in the plane of the sky, which we computed simply

[5]N.B. We do not include a cut on $(J-H)$ or $(H-K_s)$, partly for simplicity but also to remove the requirement for an H magnitude in the VIRAC2 source table. Sources can lack flux measurements in the source table in one or more of the Z, Y, J, H passbands, despite having detections in the time series in the missing band(s), if all the detections in that passband are marked as ambiguous matches, i.e. potentially matching to more than one source. An example of this is the second T dwarf listed in Table 3, for which no H band magnitude is listed in the source table but there are 3 detections in the time series, all flagged as ambiguous matches.

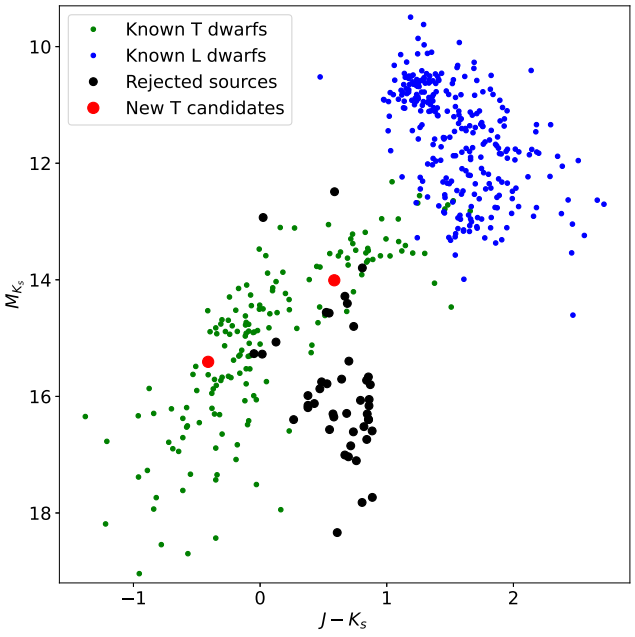

Figure 11. Colour versus absolute magnitude diagram for the sources identified in the T dwarf search. Known L dwarfs (blue points) and T dwarfs (green points) from the UltracoolSheet are overplotted, with unresolved binaries excluded. The two new discoveries with visually confirmed proper motion (large red points) lie in the same region as known T dwarfs (green points). Candidates that failed the visual inspection (black points) mostly lie below this region.

as $V_{\rm tan} = 4.74\mu/\varpi$. The UWE of valid solutions should typically be near unity, but the distribution for the 750 initial candidates was found to rise steeply at UWE > 1. Further investigation using a cross match to GCNS (see Section 4.1.3) found that bona fide nearby stars typically have $0.7 < UWE < 1.1$ in VIRAC2, though there is a tail extending to higher values. For example, VVV J165507.13-421755.8, the T5 dwarf that was missed in Section 4.1.1, has UWE = 1.48. Compared to bona fide nearby sources, candidates lacking a GCNS match have a distribution with a larger mode in UWE, corresponding to unreliable astrometric solutions in most cases.

The $V_{\rm tan}$ parameter can be used to complement the cut on proper motion (item (v) above) by removing a large number of sources with significant proper motions but over-estimated parallaxes, these typically having unusually small values of $V_{\rm tan}$ (a few km s^{-1}). Some genuine nearby stars will have unusually small tangential velocities and another small proportion will have large UWE values. We therefore used two complementary selections to capture such cases.

Selection 1: UWE < 1.2
Selection 2: UWE < 1.5 and $V_{\rm tan} > 10$ km s^{-1}

Selection 1 provided 36 candidates and Selection 2 provided 13 candidates. After visually inspecting pairs of cut-out images taken several years apart, only two candidates showed clear proper motions and these turned out to be the only two located in the 'sweet spot' where both selections are satisfied. The two mid-late T dwarf candidates are VVV J182046.14-274239.0, hereafter VVV 1820-2742, and VVV J125338.22-633947.0, hereafter VVV 1253-6339. Finder charts for these targets are provided in Appendix D. In Fig. 11, we plot the two in a colour versus absolute magnitude diagram (large red circles). For comparison, we overplot L dwarfs (blue points) and T dwarfs (green points) from the UltracoolSheet,[6] along with the candidates rejected by visual inspection (black points). Data for the two T dwarfs are given in Table 3. For VVV 1253-6339, we include colours that draw on *Spitzer* mid-infrared photometry from the Deep Galactic Legacy Infrared Mid-Plane Survey Extraordinaire survey (Deep GLIMPSE; Whitney et al. 2011), having propagated the VIRAC2 coordinates to Epoch 2012.5 and matching with a 1 arcsec cross-match radius. Care must be taken when matching VVV and *Spitzer* detections because the spatial resolution of the latter is poorer (∼2 arcsec), sometimes causing flux from more than one VVV source to be included in the beam. Inspection of the images indicates no such problem in this case though. VVV 1820-2742 was not detected by any of *Spitzer* Galactic surveys.

VVV 1820-2742 is at a distance, $d \approx 27$ pc, very similar to the early T dwarf candidate VVV 1814-2654 and it has a similar projected location within the Galactic bulge. However, the different proper motions indicate that a common origin is unlikely. The $J - H$, $H - K_s$, and $J - K_s$ colours resemble those of normal stars. Such colours suggest a spectral type of T2 to T3, based on inspection of the data provided by Kirkpatrick et al. (2021). The M_{K_s} value indicates a spectral type of T3 to T4.5, based on the data in the 2MASS passband provided by Dupuy & Liu (2012), consistent with the colours.[7]

Table 3. Data for the T dwarfs VVV 1820-2742 and VVV 1253-6339, discovered by the T dwarf search. The VIRAC2 J2000 coordinates are at epoch 2014.0 and the M_{K_s} values are computed as in Table 2.

VIRAC2 source ID	13 415 483 005 492	16 122 933 004 133
Name	VVV J1820-2742	VVV J1253-6339
RA (hms)	18 20 46.14	12 53 38.22
Dec (dms)	−27 42 39.0	−63 39 47.0
RA (°)	275.192250	193.409232
Dec (°)	−27.710837	−63.663048
l (°)	4.8711048	303.175843
b (°)	−6.137462	−0.792342
$\mu_{\alpha\cos\delta}$(mas yr^{-1})	10.0 ± 1.9	-190.7 ± 2.0
μ_δ(mas yr^{-1})	-175.9 ± 1.9	-255.9 ± 2.1
ϖ (mas)	36.8 ± 4.3	66.6 ± 6.7
d (pc)	$27.1^{+3.6}_{-2.9}$	$15.0^{+1.7}_{-1.4}$
Z	>19.5	19.77 ± 0.19
Y	17.81 ± 0.07	16.89 ± 0.01
J	16.77 ± 0.05	15.88 ± 0.01
H	16.32 ± 0.05	16.10 ± 0.01
K_s	16.18 ± 0.10	16.29 ± 0.11
M_{K_s}	$14.01^{+0.26}_{-0.29}$	$15.40^{+0.24}_{-0.25}$
$Z - J$	>2.7	3.89 ± 0.19
$Y - J$	1.04 ± 0.09	1.01 ± 0.01
$J - H$	0.45 ± 0.07	-0.22 ± 0.01
$H - K_s$	0.14 ± 0.11	-0.19 ± 0.11
$J - K_s$	0.59 ± 0.11	-0.41 ± 0.01
K_s − [3.6]	–	1.63 ± 0.15
[3.6] − [4.5]	–	0.87 ± 0.16

[6]A regularly updated compilation of data for known brown dwarfs, https://doi.org/10.5281/zenodo.10573247.

[7]The VISTA/VIRCAM filters are not identical to the 2MASS or MKO filters, which complicates the comparison. In K_s, VIRCAM closely resembles 2MASS K_s; in H, the VIRCAM, MKO and 2MASS filters are all quite similar; in J, VIRCAM resembles MKO rather than the unusually broad 2MASS J filter. By comparing VIRAC2 results with either MKO or 2MASS, as appropriate, the effects of different filter systems should be smaller than the intrinsic scatter at each spectral type.

VVV 1253-6339 is at a distance, $d \approx 15$ pc, very similar to the white dwarf VVV J141159.32-592045.7, the nearest star to be discovered by VIRAC v1 (Smith et al. 2018). The negative $J - H$, $H - K_s$, and $J - K_s$ colours and fainter M_{K_s} value indicate a later spectral type than VVV 1820-2742. Comparison with the colour data in Kirkpatrick et al. (2021) indicates a type later than T4 and the M_{K_s} value suggests a T6 or T7 type (Dupuy & Liu 2012). The $[3.6] - [4.5]$ colour is consistent with a type between T4 and T6.5, based on comparison with data in the UltracoolSheet, which were drawn mainly from Patten et al. (2006), Kirkpatrick et al. (2011), Mace et al. (2013), Kirkpatrick et al. (2019), Meisner et al. (2020a, b), Kirkpatrick et al. (2021), and Griffith et al. (2012). Taken together, these constraints imply a spectral type of ∼T6.

While these two systems are technically only candidates, their T dwarf nature is almost certain, given their colours, high proper motions and parallaxes. The only plausible alternative, in the case of VVV 1820-2742, would be an L-type subdwarf (see e.g. Zhang et al. 2017). However, this would require the parallax to be greatly overestimated. Such objects are in any case much rarer than T dwarfs. For VVV 1253-6339, the red $[3.6] - [4.5]$ colour appears to rule out the L subdwarf interpretation.

A limitation of this search is that it was difficult to confirm or reject some candidates with $\mu < 40$ mas yr^{-1} through visual inspection of the images, since the candidates are mostly quite faint and total motion over the course of the survey is small. We only report sources with obvious motion here and we also imposed a hard lower limit at $\mu = 30$ mas yr^{-1}, so it is possible that some slow-moving T dwarfs were missed.

4.1.3 $d < 50$ pc search

We performed a parallax-based search for new sources within 50 pc without any colour-based criteria. From the initial selection of ∼1.6 million candidate nearby ($\varpi > 10$ mas) VIRAC2 sources with 5σ parallax detections described in Section 4.1, we applied the following additional cuts:

(i) $\varpi > 20$ mas
(ii) $f_{amb} < 0.4$
(iii) $\Delta t > 6$ yr
(iv) $ks\_n\_det > 20$
(v) $\mu > 30$ mas yr^{-1}
(vi) UWE < 1.2
(vii) $V_{\rm tan} > 5$ km s^{-1}

Cuts (ii) to (vii) in this list are based on the same parameters that we used to select T dwarfs in Section 4.1.2. The choice of a 6 yr minimum time baseline and a maximum UWE limit of 1.2 were informed by a cross-match against GCNS (Smart et al. 2021) that also helped to identify previously known nearby systems. The cross-match was performed using a set of 1.34 million VIRAC2 sources, a subset of the initial 1.6 million candidate nearby sources with these additional criteria: $f_{amb} < 0.4$, $\Delta t > 0.5$ yr, and $ks\_n\_det > 20$. A small cross-match radius of 0.5 arcsec was used to minimize the number of chance alignments, having first propagated all GCNS source coordinates back from the *Gaia* reference epoch at 2016.0 to the VIRAC2 reference epoch at 2014.0. This cross-match yielded 2178 matches. All of the matched sources have $\Delta t > 4$ yr and ∼99 per cent have $\Delta t > 6$ yr.

The distribution of UWE for matched sources is shown by the solid red line in Fig. 12. These bona fide nearby stars ($d < 100$ pc) typically have proper motions $\mu > 30$ mas yr^{-1}. The other lines in Fig. 12 show the distributions of UWE for (i) unmatched VIRAC2 sources (dashed blue line), (ii) unmatched VIRAC2 sources with $\mu > 30$ mas yr^{-1} (dashed magenta line) and (iii) unmatched VIRAC2 sources with $\mu > 200$ mas yr^{-1} (solid black line). We see that bona fide nearby stars have a peak at UWE = 0.9, slightly above the typical value of 0.85 for the VIRAC2 catalogue as a whole (see Fig. 6). The larger typical values of UWE for unmatched sources show that most of them have unreliable astrometric solutions. Our cut at UWE = 1.2 should include most bona fide nearby stars, whilst excluding the bulk of the unreliable solutions. Erroneous astrometric solutions with large proper motions are frequently due to mis-matches in the time series, i.e. a fit to two different stars. Encouragingly, the solid black line in Fig. 12 shows a small secondary peak just below unity. We can presume this feature corresponds to genuine new high proper motion stars that are not in GCNS.

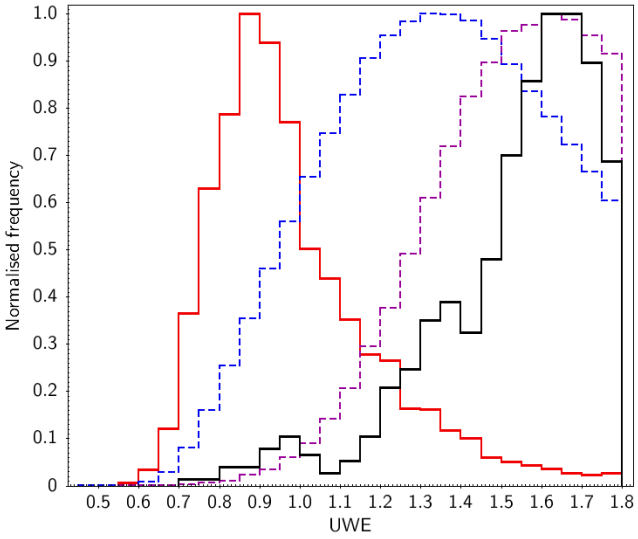

Figure 12. Normalised distributions of the VIRAC2 UWE parameter for VIRAC2 candidate nearby sources ($\varpi > 10$ mas) having a counterpart in GCNS (red line) or not (other lines). The selections in the latter case are (i) all sources (dashed blue line); (ii) $\mu > 30$ mas yr^{-1} (dashed purple line); and (iii) $\mu > 200$ mas yr^{-1} (black line). Sources with no GCNS match typically have incorrect parallaxes and larger UWE values than GCNS matches, though the $\mu > 200$ mas yr^{-1} subset shows a small peak at UWE ≈ 1, suggesting scope for new discoveries.

Having justified criteria (ii) to (vi), cut (vii) on $V_{\rm tan}$ was necessary to reduce the number of VIRAC2 candidates to a manageable level for individual inspection. Without it, cuts (i) to (vi) leave 10 526 candidates with $\varpi > 20$ mas. A 5 km s^{-1} cut was imposed in order to retain slow moving stars such as the nearby white dwarf VVV J141159.32-592045.70 ($V_{\rm tan}$=7 km/s) which was discovered with VIRAC v1 (Smith et al. 2018). After applying this cut, we had 628 candidates. This selection had 150 matches in GCNS, using a 0.5 arcsec matching radius at epoch 2014.0 as above, which left 478 new candidate nearby sources. This is still a large number for visual inspection so we decided to increase the parallax significance threshold from $\varpi/\sigma_\varpi > 5$ to $\varpi/\sigma_\varpi > 7$. This left 89 candidates for assessment, after excluding the three T dwarf candidates already listed in Tables 2 and 3.

In a plot of σ_ϖ versus ϖ (not shown), these 89 candidates split into two groups: (i) a smaller group of mainly composed of brighter sources ($13.5 < K_s < 16$) with smaller parallaxes and errors ($20 < \varpi/{\rm mas} < 50$, $1 < \sigma_\varpi/{\rm mas} < 6$) that we might expect to be accurate solutions; (ii) a larger group of fainter sources ($K_s > 16$)

mostly having larger parallaxes and errors ($\varpi > 60$ mas, $\sigma_\varpi > 7$ mas) in which we would expect inaccurate solutions to predominate. We visually inspected pairs of cut-out images taken several years apart to confirm the high proper motions, using the SAOIMAGE DS9 software to mark the positions expected at the date of observation. Marking the expected positions was necessary because there were cases where there was a discernible proper motion that differed from the VIRAC2 values, owing to the effect of blending (or blending and stellar variability) on the source matching and the astrometric solution. After this check, only 12 nearby candidates with visually confirmed high proper motions remained. An additional check on the astrometric solutions was made by plotting RA versus time and Dec versus time, to confirm the expected linear trends.

The 12 candidate nearby sources are listed in Table 4, and finder charts for some are provided in Appendix D. The final column contains an indicative UCD spectral type based on the M_{K_s} versus spectral-type relation in Dupuy & Liu (2012), provided that the colours and absolute magnitude are consistent. The best-fitting subtype is shown in brackets to indicate that there is significant uncertainty. A simple question mark indicates that colours are not consistent with a UCD interpretation, whereas 'L(?)' type indicates indicates a UCD for which M_{K_s} is fainter than the usual range for L0-T2 types.

We caution that verification of high proper motion does not guarantee that the parallaxes are correct. E.g. the 150 sources with $\varpi > 20$ mas and a match in GCNS include four cases where the VIRAC2 parallax is larger than the *Gaia* parallax by a factor between two and three, corresponding to discrepancies at the 3.3σ to 4.5σ level. We tried inspecting plots of the annual parallactic motion in RA and Dec, after subtracting the proper motion. In a few cases with high parallax significance it was possible to clearly confirm the motion by phase-folding the time series on a 1 yr period and then binning the detections by phase to reduce the large scatter on individual points. More often though, plots of parallax fits with below $\sim 10\sigma$ significance (not shown) appear plausible rather than compelling, due to large error bars and the fact that the observing season for a given source often has a phase coverage of only about half a year. By way of cautionary examples, it initially appeared that we might have 14 bona fide new nearby sources where the proper motion was visually confirmed in the images. However, two of these systems had unusual properties and they were ruled out on further investigation of all available information, including the plots of position versus time. Details of these failure modes are given in Appendix B, in case they are relevant to further work with VIRAC2.

In Table 4, we see that all sources are in the range $10.8 < M_{K_s} < 13.9$ (neglecting uncertainties in parallax and photometry). In this range we would expect to find L dwarfs, T dwarfs, and white dwarfs. Nine of the 12 sources were also found in our focussed search for red UCDs, discussed in Section 4.1.4. To avoid repetition, we discuss only the other three sources here: source nos. 1, 8 and 9.

To provide more information, we cross-matched the sources in Table 4 with the second data release of DECaPS, Saydjari et al. 2023), the deepest optical survey available for the southern Galactic plane. A positional match within 0.5″cross-match radius was required after propagating the VIRAC2 coordinates to the mean observation date of the DECaPS catalogue entry. All 12 sources except source no. 9 had a catalogue match.

We also cross-matched the sources in Table 4 with the *Spitzer* GLIMPSE I, GLIMPSE II, GLIMPSE 3D, Deep GLIMPSE,

Table 4. Additional new sources within 50 pc of the Sun. Coordinates are for Epoch 2014.0, Equinox J2000.0. Approximate distances and M_{K_s} values are based on the reciprocal of parallax. Errors on fluxes are available in the VIRAC2 source table. Nominal spectral types, based mainly on M_{K_s}, are indicated in the 'SpT' column, with the best-fitting subtype in brackets (see the main text).

#	Source ID	VVV designation	RA (°)	Dec (°)	$\mu_{\alpha*}$ (mas yr^{-1})	μ_δ (mas yr^{-1})	ϖ (mas)	d (pc)	K_s	M_{K_s}	$Z-J$	$Y-J$	$J-H$	$H-K_s$	$J-K_s$	SpT
1	16 064 415 000 927	VVV J121047.63-622729.2	182.69846	−62.4581	−152.1 ± 1.6	31.1 ± 1.7	35.0 ± 4.2	28	16.13	13.84			1.32	1.15	2.47	L(?)
2	16 028 292 006 473	VVV J133647.47-614648.4	204.19778	−61.78012	123.4 ± 0.4	54.0 ± 0.4	31.5 ± 1.3	31	14.58	12.06	2.50	1.19	0.84	0.51	1.36	L(6)
3	15 983 628 001 410	VVV J140116.84-605554.0	210.32018	−60.93168	−130.4 ± 0.7	−132.9 ± 0.7	30.2 ± 2.1	33	15.15	12.55	2.99	1.47	1.25	0.82	2.07	L(8)
4	16 081 224 003 667	VVV J140705.59-624656.0	211.77328	−62.78223	−153.8 ± 0.7	−123.9 ± 0.9	30.9 ± 2.2	32	15.39	12.84	2.43	1.05	0.96	0.56	1.51	L(9)
5	15 214 987 007 021	VVV J163823.65-484211.5	249.59856	−48.70319	0.6 ± 0.5	−87.5 ± 0.5	28.3 ± 1.4	35	14.17	11.43	2.52	1.21	0.83	0.54	1.37	L(3)
6	14 394 269 006 924	VVV J172522.93-382122.1	261.34555	−38.35615	−34.0 ± 0.9	−106.7 ± 0.8	28.0 ± 2.9	35	15.05	12.29	1.98	0.87	0.74	0.42	1.17	L(7)
7	13 218 726 001 114	VVV J172821.46-254333.2	262.08942	−25.72589	105.8 ± 2.1	−18.3 ± 2.0	32.2 ± 4.0	31	15.63	13.15	2.77	1.14	0.84	0.60	1.44	T(1)
8	13 140 915 004 830	VVV J173302.42-245559.9	263.2601	−24.93331	−6.0 ± 1.1	−30.8 ± 1.1	20.4 ± 2.8	49	14.37	10.94	1.46	0.78	0.94	0.48	1.42	?
9	12 829 649 008 054	VVV J174337.03-215018.1	265.90427	−21.83836	−71.1 ± 2.2	−32.4 ± 2.5	34.2 ± 4.4	29	15.77	13.47	0.96	0.38	0.56	0.32	0.88	?
10	14 222 340 003 203	VVV J180133.75-362315.0	270.39062	−36.38749	108.5 ± 0.7	−47.0 ± 0.8	21.2 ± 1.4	47	14.19	10.82	2.49	1.18	0.76	0.59	1.34	L(1)
11	14 124 045 003 421	VVV J180450.03-351920.2	271.20844	−35.32227	−8.7 ± 0.7	−145.6 ± 0.8	20.5 ± 1.6	48	15.04	11.61		1.53	1.15	0.85	2.00	L(4)
12	13 673 522 002 486	VVV J181736.80-302618.9	274.40332	−30.43858	−259.4 ± 0.4	−133.9 ± 0.4	22.0 ± 1.0	45	14.33	11.04	2.30	1.03	0.59	0.48	1.07	L(2)

GLIMPSE Proper, and ApoGLIMPSE mid-infrared Galactic surveys (Benjamin et al. 2003; Churchwell et al. 2009; Whitney et al. 2011; Benjamin et al. 2015, 2016). A 1 arcsec cross-match radius was used, after first propagating the VIRAC2 coordinates to suitable dates when the VVV area was observed in each survey. Six of the 12 sources in Table 4 have no match, including source nos. 8 and 9, and a further two sources with matches (listed in Section 4.1.4) have unreliable *Spitzer* photometry because inspection of the images indicates that two VVV sources are blended into a single *Spitzer* source. However, four of the 12 sources in Table 4 have unblended matches in the $I1$ (3.6 μm) and $I2$ (4.5 μm) filters: source nos. 1, 3, 4, and 6.

Source no. 1 (VVV J121047.63-622729.2, hereafter VVV 1210-6227) has $M_{K_s} = 13.84$, corresponding to a T3 type, but its J-H and H-K_s colours are unusually red even for an L dwarf and far too red for a T3 type. The *Spitzer* matches give us the colours $K_s - [3.6] = 1.63 \pm 0.13$ and $[3.6] - [4.5] = 0.31 \pm 0.22$, which are most consistent with a late L type. DECaPS has catalogued detections in i, z, and y filters and the colour $z - J = 2.41$ is also more consistent with an L type than a T type, from comparison with typical UCD colours given in Carnero Rosell et al. (2019) for Dark Energy Camera and VISTA photometry. Inspection of the images shows no sign of the source in i however: the entry was based on a single detection, whereas most bona fide entries have two or more detections. One possibility is that VVV 1210-6227 is a young late-type L dwarf with very low gravity, given that these sources typically have redder near infrared colours than normal field L dwarfs (Faherty et al. 2016) and their M_{K_s} values appear to extend into the T dwarf range (Liu, Dupuy & Allers 2016), similar to young planets such as HR8799b, HR8799d, and 2MASS 1207-3932b (Chauvin et al. 2004; Ducourant et al. 2008; Marois et al. 2008). Alternatively, if the parallax is overestimated by $\sim 2.5\sigma$ then it could simply be a late L dwarf with unusually red colours. The BANYANΣ software tool (Gagné et al. 2018) finds a 91 per cent probability that that the system is a field object, rather than member of a known young moving group. However, a number of very low gravity L dwarfs are known that are not members of known young moving groups (Faherty et al. 2016; Liu et al. 2016) so this check is not conclusive.

Source no. 8 (VVV J173302.42-245559.9) is an interesting case. The M_{K_s} value is in the range for L dwarfs and most of the VIRAC2 colours are red, consistent with this. However, the $Z - J$ colour (and to a lesser extent the $Y - J$ colour) is unusually blue for such sources. The DECaPS data show that the optical colours are also relatively blue: $r - i = 1.40, i - z = 0.79$. Some possible explanations for this transition from bluer optical colours to redder near infrared colours are (i) a blend of a UCD and a more distant, optically brighter star that does not contribute significantly to the astrometric solution due to being fainter in the infrared; (ii) a white dwarf + L dwarf binary pair.

Source no. 9 (VVV J174337.03-215018.1) has $M_{K_s} = 13.47$, in the range for early T dwarfs. However, the blue $Z - J$ and $Y - J$ colours are not consistent with a brown dwarf: even very metal-poor UCDs have $Y - J > 0.5$ (Zhang et al. 2018), suggesting that it may be a white dwarf. Unfortunately, source no. 9 is just outside the DECaPS footprint. The only available optical detections are a single passband datum from *Gaia* DR3 ($G = 20.36$), without a parallax, and a y band detection in the second data release of the Panoramic Survey Telescope and Rapid Response System (Pan-STARRS1 DR2; Chambers et al. 2016; Flewelling et al. 2020). The latter detection adds little to the VIRAC2 photometry but the colour $G - J = 3.71$ and absolute magnitude $M_G = 18.06$ are not in the range occupied by typical UCDs (Reylé 2018). The absolute magnitude is also very faint for a white dwarf (see e.g. Golovin et al. 2024). This source therefore appears to be an unusual system, provided that the parallax measurement is correct.

4.1.4 Red UCD search

Finally, we searched for new red UCDs using cuts on absolute magnitude and colour that should include sources with spectral types in the L0 to T2 range, though some late M-type UCDs can be expected to scatter in. We began with the ∼1.6 million candidate nearby VIRAC2 sources ($\varpi > 10$ mas, i.e. within ∼100 pc) with 5σ parallax detections that were selected in Section 4.1 and we then applied the following initial cuts:

(i) $M_{K_s} > 10.4$
(ii) $Y - J > 0.8$
(iii) $J - K_s > 0.9$

This yielded 262 903 sources, so it was clear that additional cuts are needed to remove the numerous reddened distant stars in the Galactic plane with incorrect parallax estimates. We performed three selections from this set using f_{amb}, UWE, Δt, μ and $V_{\rm tan}$ to define quality cuts that are likely to include most genuine nearby sources. These selections (denoted 3a, 3b, and 4) complement the colour-blind 50 pc search in Section 4.1.3 mainly by including sources at $d = 50$ to 100 pc and sources with only 5σ parallax significance, as opposed to 7σ previously.

Selections 3a and 3b first required $V_{\rm tan} > 10$ km s^{-1}, which reduced the sample from 262 903 sources to 619. A cross-match to GCNS with a 0.5 arcsec cross-match radius at epoch 2014.0 coordinates, found that 17 of these were known, leaving 602 potentially new candidates.

Selection 3a then applied these cuts:

(i) $\Delta t > 3$ yr
(ii) $f_{\rm amb} < 0.1$
(iii) UWE < 1.5

This yielded 54 candidates, of which 49 were visually confirmed as high proper motion sources. Of the remaining five, three were definite false positives and two cases were unclear due to low proper motion.

Selection 3b complemented 3a by relaxing the threshold on $f_{\rm amb}$, whilst tightening the constraint on UWE:

(i) $\Delta t > 3$ yr
(ii) $0.1 < f_{\rm amb} < 0.4$
(iii) UWE < 1.2

This yielded eight candidates, only one of which, VVV J181549.13-234845.1, passed the visual proper motion check. This is in fact a known L dwarf, LTT 7251 B (= HD 167 359 B), discovered by Smith et al. (2018) using VIRAC v1 via a match of high proper motion sources to stars in the Tycho-*Gaia* Astrometric Solution (TGAS) catalogue (Michalik, Lindegren & Hobbs 2015). LTT 7251 B is not detected by *Gaia* and hence it is not in the GCNS main table. It is also not in the GCNS table of missing objects since it has no parallax in the SIMBAD data base at present. VIRAC v1 did not provide a parallax but VIRAC2 now does: $\varpi = 29.7 \pm 3.6$ mas. This is consistent with the *Gaia* DR3 value measured for the G8-type primary, LTT 7251 A: $\varpi = 26.54 \pm 0.02$ mas.

Selection 4 complemented selections 3a and 3b by reducing the threshold value of $V_{\rm tan}$ from 10 to 5 km s^{-1}. To avoid including a very large number of false positives, this required us to impose tight

constraints on all the other data quality parameters and apply a proper motion cut also:

(i) $\Delta t > 6$ yr
(ii) $f_{amb} < 0.1$
(iii) UWE < 1.2
(iv) $\mu > 30$ mas yr^{-1}
(v) $5 < V_{\rm tan}/{\rm kms}^{-1} < 10$

Selection 4 yielded 19 candidates, six of which were visually confirmed as (relatively) high proper motion sources. Of the remainder, 11 were clearly erroneous and two were unconfirmed due to the modest proper motions and blending.

In Table 5, we list the 56 red UCD candidates from selections 3a, 3b, and 4 that have visually confirmed high proper motions and are not in GCNS. A colour versus absolute magnitude diagram for these sources is plotted in Fig. 13 (red stars) and VVV 1210-6227, the low-gravity late L dwarf candidate from Table 4 is also marked (purple star). Known M dwarfs (black points), L (blue points), and T dwarfs (green points) from the UltracoolSheet are overplotted for comparison.

Of the 56, nine were also found in the colour-blind 50 pc search (see Table 4) and the selection also includes the high proper motion early T dwarf candidate VVV J1814-2654 (see Table 2). We retain these sources in Table 5 to give the complete colour selection in one place. Fifty-three of the 56 sources were included in VIRAC v1, but only 15 had parallaxes in that catalogue, in which 5σ significance was required; only nine of these were listed as L dwarf candidates since the VIRAC v1 aperture photometry is less reliable than VIRAC2 DOPHOT photometry. For the 15 with parallaxes, they are all consistent between VIRAC v1 and VIRAC2. The uncertainties in VIRAC2 ϖ, $\mu_{\alpha *}$ and μ_δ are smaller by 28 per cent, 43 per cent and 45 per cent, respectively (median values). This reflects the fact that the longer time baseline of VIRAC2 improves proper motion precision more than parallax precision. A further three of the 56 sources were identified as UCDs using VIRAC v1 proper motion and colours alone (Smith et al. 2018). Such an approach could be tried with VIRAC2 but it is beyond the scope of this work. After accounting for the VIRAC v1 discoveries, including LTT 7251 B mentioned earlier, we are left with 43 new red UCD candidates. None of these systems are in the UltracoolSheet.

An indicative spectral type is given in the final column of Table 5 in a similar manner and format to Table 4, based on the M_{K_s} versus type relation. A minor change was made for source no. 32 (discussed further below) where the M_{K_s} versus spectral-type relation indicated a best-fitting type of T3: the value was changed to T2 to be more consistent with the red colours, while remaining consistent with the absolute magnitude. 'L(?)' is given in cases where there is good reason to suspect the parallax is substantially overestimated, detailed below. For LTT 7251 B (source no. 48), the known spectral type of L7 is given.

Two systems in Table 5 are binaries. VVV J163823.65-484211.5 (source no. 18) has a *Gaia* DR3 parallax, $\varpi = 26.8 \pm 1.6$ mas, very similar to the VIRAC2 value, 28.3 ± 1.4 mas. It is only a new discovery in the partial sense that it was not in the GCNS list of nearby sources, despite having a parallax in *Gaia* eDR3. Our visual inspection showed that it is part of a binary pair: there is a brighter component, *Gaia* eDR3 source 5 940 919 607 037 021 568 (VVV J163823.52-484211.7), that is included in VIRAC2 and GCNS, both of which indicate a proper motion and parallax similar to the secondary. The VIRAC2 colours and the absolute magnitudes indicate that the primary is also an L dwarf. The separation of 1.4″corresponds to ∼50 au at the 36 pc distance of the primary (using the *Gaia* DR3 parallax); this is unusually wide for a brown dwarf pair (Burgasser et al. 2007).

The second binary system is composed of VVV J182633.53-334138.3 (source no. 51) and VVV J182633.48-334138.4 (listed in GCNS). Again, the component listed in GCNS is the primary and VVV J182633.53-334138.3 is the secondary (which has only a two-parameter astrometric solution in *Gaia* DR3). The absolute magnitudes suggest spectral types near L0 and L3 for the pair. They are blended in the VVV images with a separation of only 0.63″but despite this the components have consistent parallaxes and proper motions, with values in fair agreement with the *Gaia* DR3 values for the primary. The projected physical separation of the pair is ∼28 au. Again this is unusually wide for an L dwarf pair, but seeing limited surveys such as VVV have a strong bias towards these relatively wide pairs.

From inspection of the *ks_eta* and *ks_Stetson_I* light curve indices given in the source table for the 56 red UCDs, one source, VVV J180315.34-303321.8 (source no. 38) stands out from the rest with $ks\_eta = 0.43$, $ks\_Stetson\_I = 3.6$, compared to typical values near two and zero for non-variable sources, respectively. The light curve of this source, an early L dwarf candidate, shows a slow ∼0.2 mag rise in K_s from 2010 to 2014 before stabilizing and fading slightly in later years (not shown). A few other sources in the list also show hints of slow small amplitude variability, indicating that the VIRAC2 data may be useful to study long-term photometric variations in UCDs, whether due to magnetic activity or changes in weather patterns. To our knowledge, previous studies of variability in UCDs, e.g. Vos et al. (2022), Oliveros-Gomez et al. (2022) and references therein, have only examined changes on much shorter timescales. Examination of small amplitude variability will require careful statistical analysis so we defer the topic to a future work.

We cross-matched the sources in Table 5 to the *Spitzer* Galactic survey archive tables and DECaPS in the same manner as for Table 4. In the *Spitzer* surveys 21/56 candidates had a match and 18 of these were judged to be largely unaffected by blending of multiple VVV sources in the *Spitzer* beam, from inspection of the images. The three blended cases are source nos. 7, 18, and 21. A [3.6] − [4.5] versus K_s − [3.6] two colour diagram is plotted in Fig. 14 for the 14/18 sources with detections in both mid-infrared passbands. Within the uncertainties, these 14 sources have K − [3.6] and [3.6] − [4.5] colours that are consistent with those of L dwarfs, from comparison with the relevant data from the UltracoolSheet that is also plotted. These colour ranges overlap with those of late M dwarfs and early T dwarfs. The T dwarf candidate VVV 1253-6339 and the candidate low gravity late L dwarf VVV 1210-6227 are also plotted in Fig. 14. The red [3.6] − [4.5] colour of VVV 1253-6339 supports a T dwarf nature and the colours of VVV 1210-6227 support a late L type. In the latter case, there is insufficient *Spitzer* data available on low-gravity late L dwarfs to judge how these colours are typically affected.

The DECaPS cross-match provided red optical photometry for 45 sources, see Fig. 15, though a few outlying data points (three in i and 2 in z) were removed from the two panels after inspection of the images indicated unreliable blended detections or non-detections. We see that most of the red UCD candidates in this work have $i - J$ and $z - J$ colours and absolute magnitudes that follow the expected trends, as illustrated by previously published candidates from the Dark Energy Survey (DES; Carnero Rosell et al. 2019). A few of the VIRAC2 candidates lie significantly below the expected trends, suggesting that a small number of the parallaxes may be overestimated. We caution that the absolute magnitudes plotted for the DES sample

Table 5. Red UCD candidates from VIRAC2. Coordinates are for epoch 2014.0, Equinox J2000.0. Approximate distances and M_{K_s} values are based on the reciprocal of parallax. Errors on fluxes are available in the VIRAC2 source table. Most of these are new discoveries, save for some candidates found in VIRAC v1 (see the main text). Nominal spectral types are indicated in the 'SpT' column, as in Table 4.

#	Source ID	VVV Designation	RA (°)	Dec (°)	$\mu_{\alpha*}$ (mas yr^{-1})	μ_δ (mas yr^{-1})	ϖ (mas)	d (pc)	K_s	M_{K_s}	$Z-J$	$Y-J$	$J-H$	$H-K_s$	$J-K_s$	SpT
1	16 052 453 002 106	VVV J122708.14-621420.1	186.7839	−62.2389	−36.3 ± 0.7	−11.4 ± 0.7	14.5 ± 2.0	69	14.60	10.41	2.11	0.89	0.66	0.60	1.26	L(0)
2	16 023 286 011 236	VVV J123646.95-613855.4	189.1956	−61.64873	−34.7 ± 0.5	−11.2 ± 0.5	13.3 ± 1.8	75	14.82	10.43	2.32	1.00	0.66	0.59	1.25	L(0)
3	16 054 900 003 583	VVV J125158.50-621637.9	192.99374	−62.27719	51.0 ± 1.1	−73.0 ± 1.1	21.6 ± 3.4	46	15.54	12.22	2.34	1.23	0.85	0.65	1.50	L(6)
4	16 050 114 000 271	VVV J130944.97-620825.3	197.43736	−62.14036	−318.3 ± 0.9	46.1 ± 0.9	15.7 ± 3.0	64	15.61	11.59	2.42	1.26	0.75	0.49	1.24	L(4)
5	16 127 533 006 131	VVV J131358.89-634426.4	198.49536	−63.74066	−50.0 ± 0.8	−47.1 ± 0.8	22.0 ± 2.3	46	14.80	11.51	1.93	0.86	0.55	0.47	1.03	L(4)
6	15 960 732 002 707	VVV J132919.47-603025.9	202.33112	−60.50718	−69.8 ± 0.9	80.8 ± 1.0	19.7 ± 2.6	51	15.54	12.01	1.97	1.00	0.67	0.33	1.00	L(5)
7	16 028 292 006 473	VVV J133647.47-614648.4	204.19778	−61.78012	123.4 ± 0.4	54.0 ± 0.4	31.5 ± 1.3	32	14.57	12.06	2.50	1.19	0.84	0.51	1.36	L(6)
8	15 983 628 001 410	VVV J140116.84-605554.0	210.32018	−60.93168	−130.4 ± 0.7	−132.9 ± 0.7	30.2 ± 2.1	33	15.15	12.55	2.99	1.47	1.25	0.82	2.07	L(8)
9	16 081 224 003 667	VVV J140705.59-624656.0	211.77328	−62.78223	−153.8 ± 0.7	−123.9 ± 0.9	30.9 ± 2.2	32	15.38	12.84	2.43	1.05	0.96	0.56	1.51	L(9)
10	15 895 686 003 323	VVV J142226.89-591831.0	215.61203	−59.30861	−54.4 ± 0.7	−40.0 ± 0.7	16.9 ± 2.4	59	15.49	11.63	2.28	1.03	0.71	0.49	1.20	L(4)
11	16 028 385 004 618	VVV J143132.70-614527.2	217.88625	−61.75756	−23.8 ± 0.5	−29.7 ± 0.5	18.9 ± 1.9	53	14.92	11.30	2.38	1.12	0.80	0.53	1.34	L(3)
12	15 786 418 001 139	VVV J154206.53-572529.8	235.52722	−57.42495	−26.3 ± 1.1	−28.6 ± 1.0	14.7 ± 2.6	68	15.50	11.33	2.47	1.07	0.69	0.45	1.14	L(3)
13	15 625 547 005 863	VVV J155405.53-544536.3	238.52303	−54.76008	−36.0 ± 0.7	−67.4 ± 0.6	14.1 ± 2.3	71	15.11	10.86	2.51	1.25	0.89	0.64	1.53	L(1)
14	15 694 314 006 505	VVV J155946.54-555039.7	239.94391	−55.84435	−102.5 ± 0.8	−101.4 ± 0.8	13.2 ± 2.0	76	15.37	10.97	2.48	1.20	0.68	0.50	1.18	L(2)
15	15 298 621 003 341	VVV J161328.24-495552.9	243.36765	−49.93135	−45.2 ± 0.8	−3.9 ± 0.8	16.3 ± 2.7	61	15.30	11.36	2.31	1.14	0.70	0.59	1.29	L(3)
16	15 363 256 005 368	VVV J161802.53-504842.3	244.51053	−50.81176	−61.2 ± 0.6	−152.2 ± 0.6	17.8 ± 1.7	56	15.11	11.37	2.52	1.32	0.92	0.63	1.56	L(3)
17	15 312 381 006 935	VVV J162816.50-500635.8	247.06874	−50.10994	26.5 ± 1.5	−17.2 ± 1.2	20.0 ± 3.6	50	15.66	12.16	2.75	1.36	0.90	0.49	1.39	L(6)
18	15 214 987 007 021	VVV J163823.65-484211.5	249.59856	−48.70319	0.6 ± 0.5	−87.5 ± 0.5	28.3 ± 1.4	35	14.17	11.38	2.52	1.21	0.83	0.54	1.37	L(3)
19	15 168 695 001 226	VVV J163953.34-480440.6	249.97226	−48.07795	36.7 ± 0.6	−30.1 ± 0.6	19.3 ± 1.8	52	14.09	10.52	2.56	1.28	0.86	0.54	1.40	L(0)
20	13 910 884 004 131	VVV J170513.58-325803.3	256.3066	−32.96757	−130.4 ± 1.4	−176.1 ± 1.2	23.0 ± 3.8	43	15.56	12.37	2.53	1.31	0.74	0.58	1.32	L(7)
21	14 758 019 000 425	VVV J170533.90-424519.7	256.39124	−42.75546	35.2 ± 1.8	18.0 ± 1.7	30.2 ± 5.0	33	16.22	13.62	2.49	1.40	0.88	0.65	1.53	L(?)
22	14 680 939 001 576	VVV J170743.15-414702.9	256.92978	−41.78413	−2.9 ± 0.7	−92.1 ± 0.7	15.6 ± 2.3	64	15.21	11.18	1.95	0.84	0.61	0.42	1.03	L(2)
23	14 308 244 000 412	VVV J172204.74-372553.2	260.51974	−37.43145	68.5 ± 1.0	17.8 ± 1.0	23.9 ± 3.5	42	15.97	12.87	2.42	1.06	1.14	0.67	1.81	L(9)
24	14 394 269 006 924	VVV J172522.93-382122.1	261.34555	−38.35615	−34.0 ± 0.9	−106.7 ± 0.8	28.0 ± 2.9	36	15.05	12.29	1.98	0.87	0.74	0.42	1.17	L(7)
25	13 218 726 001 114	VVV J172821.46-254333.2	262.08942	−25.72589	105.8 ± 2.1	−18.3 ± 2.0	32.2 ± 4.0	31	15.61	13.15	2.77	1.14	0.84	0.60	1.44	T(1)
26	12 956 633 004 119	VVV J174619.15-230825.6	266.5798	−23.14046	114.1 ± 2.5	−12.8 ± 2.4	20.9 ± 3.9	48	15.68	12.28	1.76	0.98	0.68	0.53	1.21	L(6)
27	14 521 323 002 380	VVV J175228.62-395300.3	268.11926	−39.88342	15.7 ± 0.7	−272.9 ± 0.7	11.5 ± 1.4	87	15.24	10.54	2.24	1.03	0.64	0.47	1.11	L(0)
28	14 377 969 003 025	VVV J175454.11-381356.3	268.72543	−38.23231	22.6 ± 2.3	−101.6 ± 2.4	24.7 ± 4.2	40	16.21	13.18	2.14	0.89	0.62	0.38	1.00	L(?)
29	14 545 907 003 369	VVV J175519.51-401056.0	268.8313	−40.18223	−16.0 ± 0.8	−90.2 ± 0.8	10.1 ± 1.5	99	15.60	10.63	2.27	1.19	0.78	0.58	1.36	L(1)
30	12 952 563 001 044	VVV J175534.06-230515.8	268.89194	−23.08773	−14.0 ± 1.8	−43.5 ± 1.6	23.7 ± 4.4	42	15.02	11.90	1.99	0.81	0.74	0.56	1.29	L(5)
31	14 042 109 008 844	VVV J175906.92-342531.3	269.77884	−34.42537	35.8 ± 0.9	−37.3 ± 0.9	12.1 ± 1.9	82	15.43	10.86	2.04	0.90	0.69	0.39	1.08	L(1)
32	13 014 014 002 076	VVV J175920.68-234045.3	269.83618	−23.67924	45.9 ± 2.1	5.1 ± 1.9	31.7 ± 5.4	32	16.14	13.65	2.34	1.12	0.73	0.51	1.24	T(2)
33	13 710 336 009 213	VVV J175955.42-305014.8	269.98093	−30.83745	56.4 ± 0.8	−115.7 ± 0.9	12.9 ± 1.8	78	15.01	10.57	2.24	1.02	0.74	0.41	1.14	L(1)
34	14 660 608 000 029	VVV J175959.38-413153.5	269.99744	−41.53152	−13.4 ± 0.9	−114.8 ± 0.9	12.2 ± 2.0	82	15.60	11.04	1.95	0.84	0.58	0.43	1.01	L(2)
35	13 820 931 005 795	VVV J180123.11-320007.0	270.34628	−32.00194	−12.3 ± 1.0	−73.0 ± 1.0	12.8 ± 2.0	78	15.29	10.83	1.90	0.82	0.67	0.37	1.03	L(1)
36	14 222 340 003 203	VVV J180133.75-362315.0	270.39062	−36.38749	108.5 ± 0.7	−47.0 ± 0.8	21.2 ± 1.4	47	14.18	10.82	2.49	1.18	0.76	0.59	1.34	L(1)
37	13 685 769 012 201	VVV J180315.34-303321.8	270.8139	−30.55605	−24.3 ± 0.7	−245.8 ± 0.8	17.3 ± 1.4	58	14.42	10.61	1.98	0.86	0.66	0.41	1.08	L(1)
38	14 124 045 003 421	VVV J180450.03-351920.2	271.20844	−35.32227	−8.7 ± 0.7	−145.6 ± 0.8	20.5 ± 1.6	49	15.05	11.61		1.53	1.15	0.85	2.00	L(4)
39	13 566 997 000 219	VVV J180736.70-291700.1	271.90292	−29.28336	−59.6 ± 4.7	−45.2 ± 3.5	50.7 ± 9.4	20	16.09	14.62	2.50	0.83	0.51	0.54	1.05	L(?)
40	13 710 359 003 254	VVV J180804.69-304948.6	272.01956	−30.83018	4.7 ± 0.6	−164.4 ± 0.6	19.9 ± 1.2	50	14.97	11.46	2.40	1.04	0.67	0.51	1.18	L(3)
41	14 496 793 000 682	VVV J180847.83-393713.4	272.1993	−39.62039	−38.8 ± 0.9	2.9 ± 0.9	11.3 ± 2.2	89	15.48	10.74	2.20	1.04	0.63	0.47	1.09	L(1)
42	12 686 363 006 518	VVV J180927.63-202725.3	272.36514	−20.45704	55.7 ± 0.8	−3.4 ± 0.7	10.4 ± 2.0	96	15.52	10.61	2.37	1.12	0.73	0.59	1.32	L(1)
43	14 119 964 002 532	VVV J180941.71-351601.9	272.42377	−35.2672	−104.3 ± 1.8	−81.0 ± 2.0	18.1 ± 3.5	55	16.20	12.49		1.09	0.99	0.68	1.67	L(7)

Table 5 – *continued*

#	Source ID	VVV Designation	RA (°)	Dec (°)	$\mu_{\alpha*}$ (mas yr^{-1})	μ_δ (mas yr^{-1})	ϖ (mas)	d (pc)	K_s	M_{K_s}	$Z-J$	$Y-J$	$J-H$	$H-K_s$	$J-K_s$	SpT
44	14 255 135 000 834	VVV J181104.13-364709.7	272.7672	−36.78602	−6.2 ± 1.0	−36.5 ± 0.9	14.4 ± 1.9	69	15.53	11.33	2.23	0.98	0.63	0.49	1.13	L(3)
45	13 165 603 009 949	VVV J181231.37-251351.7	273.1307	−25.23102	−19.7 ± 0.7	−28.3 ± 0.7	10.9 ± 1.5	92	15.51	10.70	1.90	0.81	0.62	0.38	1.00	L(1)
46	13 931 562 003 722	VVV J181445.46-331032.0	273.68942	−33.17556	−2.6 ± 1.3	−34.2 ± 1.4	15.3 ± 2.8	65	16.20	12.13		1.24	0.98	0.76	1.74	L(6)
47	13 333 546 009 625	VVV J181453.17-265453.6	273.72156	−26.91488	−235.1 ± 2.1	−446.7 ± 2.2	36.4 ± 4.2	28	15.80	13.60		1.20	0.93	0.56	1.49	T(2)
48	13 030 445 003 531	VVV J181549.13-234845.1	273.95468	−23.81254	76.3 ± 2.2	−174.5 ± 2.3	29.7 ± 3.6	34	15.71	13.07	2.68	1.32	0.66	0.70	1.36	L7
49	13 304 881 005 250	VVV J181728.87-263606.4	274.37027	−26.60177	11.4 ± 1.0	−63.7 ± 1.1	10.8 ± 2.0	93	15.25	10.42	2.06	0.89	0.60	0.44	1.04	L(0)
50	13 673 522 002 486	VVV J181736.80-302618.9	274.40332	−30.43858	−259.4 ± 0.4	−133.9 ± 0.4	22.0 ± 1.0	46	14.33	11.04	2.30	1.03	0.59	0.48	1.07	L(2)
51	13 976 651 001 568	VVV J182633.53-334138.3	276.6397	−33.69398	−48.0 ± 1.4	−99.7 ± 1.6	22.6 ± 2.5	44	14.54	11.35		1.25	0.79	0.69	1.48	L(3)
52	13 382 741 000 588	VVV J182959.78-272446.4	277.49908	−27.41289	16.7 ± 0.7	−74.5 ± 0.7	11.8 ± 1.5	85	15.07	10.43	1.63	0.82	0.54	0.48	1.03	L(0)
53	13 435 995 001 647	VVV J183208.77-275804.3	278.03653	−27.96786	62.1 ± 1.1	−13.1 ± 1.2	12.6 ± 2.2	79	15.60	11.10	2.32	1.08	0.57	0.43	1.00	L(2)
54	13 145 182 001 396	VVV J183303.00-245943.5	278.2625	−24.99543	−104.1 ± 0.7	1.7 ± 0.7	16.1 ± 1.6	62	15.12	11.15	2.38	1.10	0.69	0.49	1.17	L(2)
55	13 493 343 002 304	VVV J183326.20-283243.9	278.35916	−28.54553	−39.7 ± 0.5	−110.6 ± 0.5	15.7 ± 1.2	64	14.65	10.62	2.02	0.92	0.57	0.43	1.00	L(1)
56	12 993 638 002 107	VVV J183608.67-232842.2	279.03613	−23.47839	−57.3 ± 1.0	−3.0 ± 0.9	13.0 ± 2.1	77	15.46	11.03	1.76	0.80	0.60	0.36	0.96	L(2)

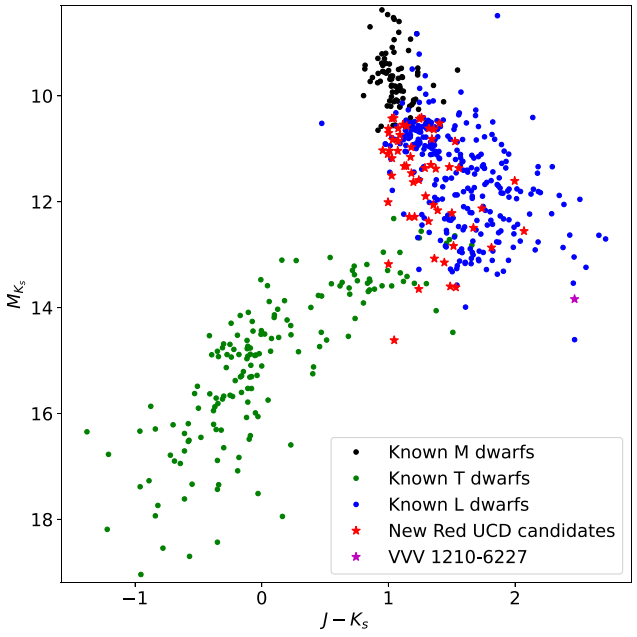

Figure 13. Colour versus absolute magnitude diagram for the 56 red UCD candidates identified by our search (red stars). The low gravity late L dwarf candidate VVV 1210-6227 is also plotted (purple star). Known late M dwarfs (black points), L dwarfs (blue points) and T dwarfs (green points) from the UltracoolSheet are overplotted, with unresolved binaries excluded.

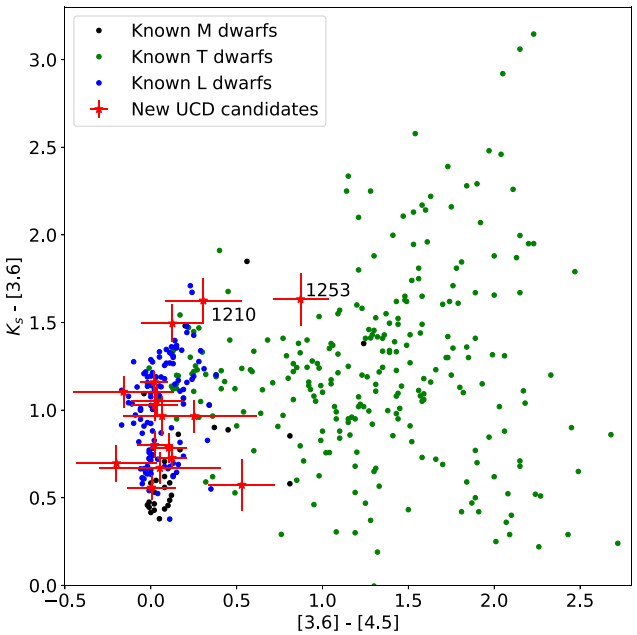

Figure 14. Two colour diagram incorporating *Spitzer* photometry. Red stars mark the new VIRAC2 UCD candidates with 3.6 and 4.5 μm detections in this work, including the low gravity late L dwarf candidate VVV 1210-6227 from Table 4 and the T dwarf candidate VVV 1253-6339 from Table 3. Known late M dwarfs (black points), L dwarfs (blue points), and T dwarfs (green points) from the UltracoolSheet are overplotted, with unresolved binaries excluded.

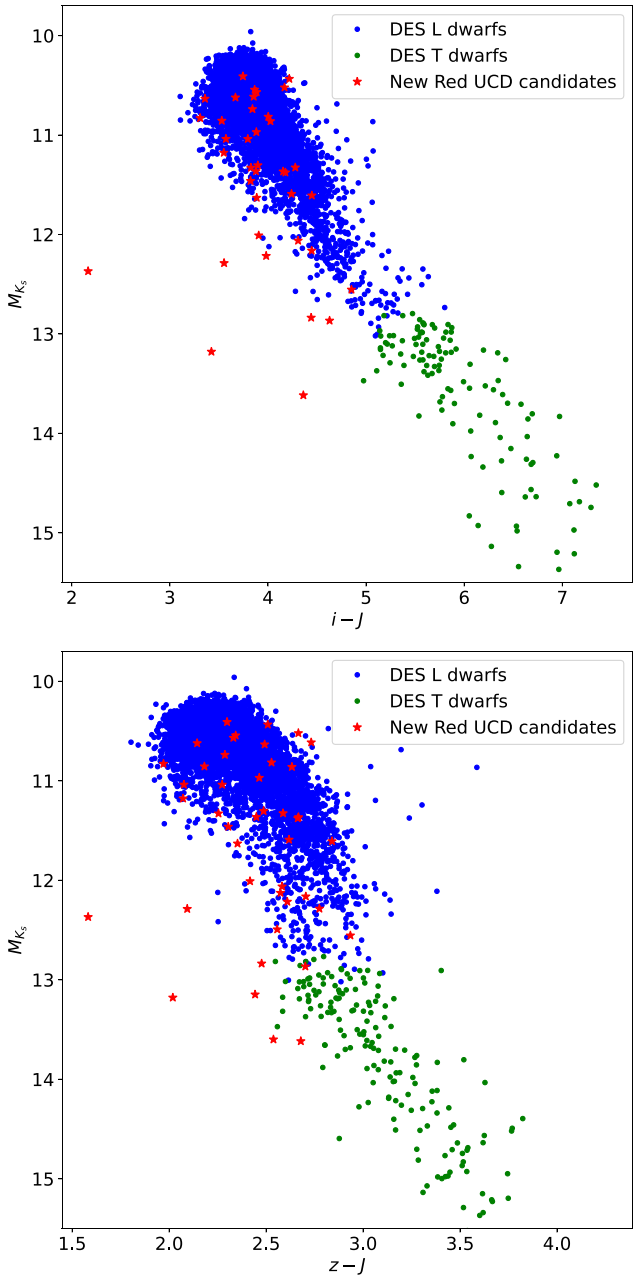

Figure 15. Colour versus absolute magnitude diagrams incorporating DECaPS photometry. Red stars mark the new VIRAC2 UCD candidates with DECaPS counterparts. L dwarf candidates (blue points) and T dwarf candidates (green points) from DES (Carnero Rosell et al. 2019) are also plotted. That study did not provide parallaxes, so the M_{K_s} values for the blue and green points are photometric estimates.

are only photometric estimates based on likely spectral types inferred from multifilter photometry, not parallax measurements. Inspection of similar plots using data from the UltracoolSheet (which provides parallaxes and Pan-STARRS photometry in somewhat different i and z filters) suggests that the actual vertical spread in M_{K_s} is likely to be larger than the blue and green data points suggest because the intrinsic spread of the UCD population is not fully captured.

Source no. 20 (VVV J170513.58-325803.3) is the most significant blue outlier in Fig. 15, with $i-J$ and $z-J$ colours inconsistent with a typical UCD. However, the DECaPS image profiles show signs of possible blending or distortion and the VIRAC2 colours are typical of an L dwarf so we retain it as a candidate. Other outliers in Fig. 15, those with $M_{K_s} > 13$, are discussed below.

While 49 of the 56 red UCD candidates have absolute magnitudes in the range of normal L dwarfs ($10.4 < M_{K_s} < 13$), seven sources ostensibly have lower luminosities ($13 < M_{K_s} < 15$), putting them in the T dwarf range. Unfortunately, none of these have reliable *Spitzer* photometry. We have mentioned two of the seven already: (i) VVV 1814-2654 ($M_{K_s} = 13.6$) was discussed in Section 4.1.1 as an early T dwarf candidate; (ii) LTT 7251 B (source no. 48 in Table 5) was found in selection 3b. The VIRAC2 parallax of LTT 7251 B corresponds to $M_{K_s} = 13.07$ but adopting the more precise *Gaia* parallax of the primary shifts the value to $M_{K_s} = 12.83$, slightly over to the L dwarf side of the L/T boundary. LTT 7251 B was assigned a spectral type of L7 in Smith et al. (2018), where it was noted as a slightly underluminous L dwarf, attributed to the mildly metal-poor nature of the system (Casagrande et al. 2011).

In these two cases the parallaxes have 8σ significance, allowing us to have some confidence in the absolute magnitudes. Moreover, the high proper motion of VVV J1814-2654, $\mu = 505$ mas yr^{-1}, translates to $V_{\rm tan} = 66$ km s^{-1} at the nominal distance. If the source were a more distant L-type dwarf then its velocity would approach or exceed 100 km s^{-1}, a rare occurrence for nearby members of the thin disc of the Milky Way.

A third system also has 8σ parallax significance: source no. 25, VVV J172821.46-254333.2 (hereafter VVV 1728-2543) has $M_{K_s} = 13.15$, placing it near the early T/late L boundary. The VIRAC2 colours are all consistent with this interpretation. VVV 1728-2543 has DECaPS photometry in the i, z, and y filters. Inspection of the images shows no sign of a detection in i (the catalogue entry was based on a single detection) but the counterparts in z and y were confirmed. Combining the DECaPS z data and VIRAC2 J data yields a colour $z-J = 2.44 \pm 0.15$, which is slightly bluer than typical values for L/T transition objects but consistent within the error bars.

The parallaxes of the other four red sources with $M_{K_s} > 13$ have only 5σ to 6σ significance. This means that a parallax overestimate is more likely, especially given the bias imparted by our 5σ parallax threshold: the error distribution will allow sources with overestimated parallaxes to scatter into the sample, whilst sources with underestimated parallaxes can scatter out. We must therefore consider the possibility that they are in fact L dwarfs at slightly larger distances. These four sources are:

(i) VVV J175454.11-381356.3, hereafter VVV 1754-3813. With $M_{K_s} = 13.18^{+0.34}_{-0.41}$, it lies at the L/T boundary, like VVV 1728-2543. At the nominal distance, $d \approx 40$ pc, the proper motion, $\mu = 104$ mas yr^{-1}, corresponds to $V_{\rm tan} \approx 20$ km s^{-1}. This source has a rather blue VIRAC2 $Z-J$ colour: $Z-J = 2.14$, only just meeting the relaxed $Z-J = 2$ threshold adopted in our earlier T dwarf search. Moreover, DECaPS detections show that it is a clear outlier in Fig. 15, with $i-J = 3.42$ and $z-J = 2.02$. It therefore appears quite likely that this is an L-type or late M-type dwarf with overestimated parallax, though an alternative possibility is that the blue colours are due to a metal-poor nature (Zhang et al. 2018).

(ii) VVV J170533.90-424519.7, hereafter VVV 1705-4245. The absolute magnitude of $M_{K_s} = 13.62^{+0.33}_{-0.40}$ suggests a spectral type in the T0–T4 range, though our red colour selection makes a T0–T2 type more likely. At the nominal distance, $d \approx 33$ pc, the proper

motion, $\mu = 40$ mas yr^{-1}, corresponds to $V_{\rm tan} \approx 6$ km s^{-1}. DECaPS data show that it is a clear outlier in the upper panel of Fig. 15 with $i - J = 4.36$, though the colour $z - J = 2.68$ is consistent with an L/T transition object. We suspect that this is a late L-type dwarf with an overestimated parallax.

(iii) VVV J175920.68-234045.3, hereafter VVV 1759-2340. The absolute magnitude of $M_{K_s} = 13.65^{+0.34}_{-0.40}$ again suggests a spectral type in the T0–T4 range, though our red colour selection makes a T0–T2 type more likely. At the nominal distance, $d \approx 32$ pc, the proper motion, $\mu = 46$ mas yr^{-1}, corresponds to $V_{\rm tan} \approx 7$ km s^{-1}. The system is not detected in DECaPS.

(iv) VVV J180736.70-291700.1, hereafter VVV 1807-2917. The absolute magnitude of $M_{K_s} = 14.62^{+0.37}_{-0.45}$ suggests a spectral type between T3.5 and T6.5. However, the low luminosity is at odds with the red colour selection, unless the system is a very low gravity L dwarf, as we suggested for VVV J1210-6227 in Section 4.1.3. The BANYANΣ software tool finds a 99 per cent probability that this is a field object rather than a member of a young moving group, though as noted previously this is not a conclusive test of youth. At the nominal distance, $d \approx 20$ pc, the proper motion, $\mu = 75$ mas yr^{-1}, corresponds to $V_{\rm tan} \approx 7$ km s^{-1}. The system lies outside the DECaPS footprint.

All four of these sources are faint, $16.0 < K_s < 16.5$, hence the modest significance of the parallax solutions. Moreover, three of the four have small tangential velocities of 6 or 7 km s^{-1}, if located at their nominal distances. These velocities are unremarkable individually but taken together they are smaller than is typical of L or T dwarfs in the local field (e.g. Schmidt et al. 2010; Seifahrt et al. 2010; Burningham et al. 2013). This gives us reason to suspect that VVV 1705-4245, VVV 1759-2340, and VVV 1807-2917 are in fact L dwarfs with overestimated parallaxes. In particular, VVV 1807-2917 has the largest parallax uncertainty in Table 5, $\sigma_{\varpi} = 9.4$ mas, approximately a factor of 2 larger than the other three candidates despite their similar brightness. This, coupled with the mismatch between colour and absolute magnitude, causes us to doubt the reliability of the solution even though the unit weight error, UWE = 1.06, does not indicate a problem.

While the 56 sources are not in GCNS, 13 have matches in *Gaia* DR3 within 0.5 arcsec, using VIRAC2 coordinates propagated to epoch 2016.0. Only two of these have five parameter solutions: (i) source no. 18 in Table 5 (VVV J163823.65-484211.5) has *Gaia* parallax and proper motion in close agreement with VIRAC2; (ii) source no. 52 (VVV J182959.78-272446.4) has a negative parallax in *Gaia* DR3, a much smaller proper motion and a relatively large reduced unit weight error (ruwe = 1.33 in *Gaia*, compared to UWE = 1.03 in VIRAC2). This disagreement may be due to the fact that towards the end of the VVV time series the source begins to be blended with a neighbouring star that is fainter in K_s but brighter in Z (and presumably brighter in the *GaiaG* passband also). *Gaia* DR3 includes only one of the two sources and the coordinates are offset from the forward-propagated VIRAC2 coordinates by 0.39 arcsec, at an intermediate location. Therefore, we speculate that the *Gaia* solution could be influenced by the neighbour and we retain source no. 52 as a candidate.

Pan-starrs1 DR2 and VPHAS+ DR2 (Drew et al. 2014) provide red optical detections of a few additional sources outside the DECaPS footprint, at Galactic longitudes $l > 5^{\circ}$. The 11 Pan-starrs1 matches (9 of which are not covered by DECaPS) all have red optical colours consistent with UCD status. VPHAS+ also has 11 matches, all of which have counterparts in DECaPS or Pan-starrs1. Of these, 10/11 have very red $i - J$ colours: $3.28 < i - J < 4.39$ (Vega system), consistent with a UCD nature. The 11th, VVV J131358.89-634426.4 appeared to be a bluer source with $i - J = 2.59$ and $r - i = 1.13$. However, inspection of the DECaPS images, taken several years after the VPHAS+ images, showed that this was due a blend of the UCD candidate and a bluer star that had begun to be resolved at the later epoch as the UCD moved away.

4.2 Synergies with VIVACE

Many types of variable star are prized for their well-established relationships between period and luminosity. These relationships can be exploited to determine approximate distances to those stars. Combined with positions and proper motions, five dimensions of kinematic information are available, enabling the study of the dynamics of their various populations.

Molnar et al. (2022) developed an automated variable star classification pipeline for VIRAC2β photometric time series data, thereby producing the VIrac VAriable Classification Ensemble (VIVACE) catalogue of nearly 1.3 million variable stars. Molnar et al. (2022) discuss and demonstrate the science potential of the catalogue, which is outside the scope of this work.

VIVACE was produced using VIRAC2β (see Appendix A for details), a preliminary version of the VIRAC2 catalogue based on a *Gaia* DR2 reference catalogue. The move to using *Gaia* DR3 for astrometric calibration meant a rerun of the main pipeline was necessary, and resulted in a low level of changes to the time series and an entirely new set of source IDs. It is therefore not quite as straightforward as it may seem to match between VIVACE and the VIRAC2 catalogue presented here. Variable stars in particular can be tricky astrometric targets in dense fields (for examples, see Section 3.2.3 and example 2 of Appendix B). To facilitate the exploitation of the combination of VIVACE with VIRAC2 astrometry, we felt it best to perform this matching ourselves using the additional information available in the (proprietary) VIRAC2β catalogue.

To provide the cleanest possible VIRAC2 counterparts to VIVACE sources, we started with a positional cross-match to the main source table, requiring separations less than 100 mas, and that there be only one VIRAC2 match within this radius. At 100 mas there was a clear separation in the bimodal distribution of distances to all matches within 1 arcsec. This yielded potential matches for 1338 664 VIVACE sources out of 1364 732. We further required that the number of K_s band detections in the VIRAC2 catalogue was no more than 5 per cent different to that of the VIRAC2β catalogue, leaving 1315 758 matches. The resultant mapping of VIVACE ID to VIRAC2 source ID is given in Table 6 (full version available in online data).

Of the $\approx$ 49 000 VIVACE sources without unambiguous counterparts in VIRAC2, 11.5 per cent have VIVACE variable type classification probability better than 0.9. This contrasts with 31.5 per cent in the complete VIVACE data set.

5 SUMMARY

We have undertaken a PSF fitting reduction of VVV and VVVX near-infrared images of 560 deg^2 of the southern Galactic plane and Galactic bulge. We described in detail our complete pipeline, from CASU reduced images through source detection, astrometric and photometric calibration, and time series production. Using various quality control criteria, we further reduced the raw 1.4 billion row output down to a more reliable catalogue. The resultant VIRAC2 catalogue we present provides five-parameter mean and time series

Table 6. Crossmatches of VIVACE sources to VIRAC2 sources. The full table is available in the online data.

VIVACE ID	VIRAC2 source ID
0	14793959001490
1	14797941003386
2	14797942001475
3	14793960001484
4	14793960002043
5	14793960001117
6	14793960001577
7	14789975003594
8	14789975001112
9	14793961001753
...	

astrometry, mean and time series photometry, and variability indices for 545 346 537 unique sources. Equivalent data are also provided for several hundred million additional *reject* sources. This selection does contain some interesting real sources (e.g. transients), but is highly contaminated with duplicated sources and other erroneous data and so we must stress that it should only be used with a high degree of caution. All tables are available from the ESO archive at https://archive.eso.org.

Peak astrometric performance was achieved in the $11 < K_s$ mag < 14 range, where proper motion uncertainties are typically ≈ 0.37 mas yr^{-1} per dimension and parallax uncertainties are typically around 1 mas. At $K_s = 16$, where the catalogue is still typically 90 per cent complete, astrometric uncertainties are around 1.5 mas yr^{-1} per dimension for proper motion and 5 mas for parallax. VIRAC2 astrometric uncertainties were checked against *Gaia* DR3, and externally against *HST* measurements, and found to be valid.

We performed an initial search of the VIRAC2 catalogue for nearby sources with significant parallaxes, thereby demonstrating the use of the various included quality control parameters for selecting high quality candidates. This search led to the identification of a number of new candidates in crowded Galactic star fields, including several projected in the inner Galactic bulge, where the census of nearby sources is much less complete than elsewhere. These discoveries include two new T dwarfs that are identified with high confidence and several other sources with redder colours that appear to lie close to L/T transition. In total, 26 new sources were discovered at likely distance $d < 50$ pc, including a T dwarf at $d \sim 15$ pc and two sources with relatively blue optical colours that are of uncertain nature. Further searches for nearby sources in VIRAC2 can be undertaken, including searches for fainter brown dwarfs and white dwarfs near the sensitivity limit that would rely more on proper motion than parallax.

VIRAC2 covers a region of the Milky Way in which *Gaia*, the Rubin observatory LSST and other optical surveys are essentially blind, and hence complements them superbly. It might also provide a useful early epoch for potential future Roman Space Telescope, JASMINE and GaiaNIR proper motion surveys, thereby retaining value for many years to come.

ACKNOWLEDGEMENTS

We thank the anonymous referee for their careful reading and comments.

We gratefully acknowledge the use of data from the ESO Public Survey programme IDs 179.B-2002 and 198.B-2004 taken with the VISTA telescope and data products from the CASU and the VSA and the ESO Science Archive. VVV and VVVX data are published in the ESO Science Archive in the data collections identified by the following DOIs: https://doi.eso.org/10.18727/archive/67 and https://doi.eso.org/10.18727/archive/68.

This work has made use of the University of Hertfordshire's high-performance computing facility, we are grateful to its architects and maintainers.

This paper made use of the Whole Sky Database (wsdb) created and maintained by Sergey Koposov at the Institute of Astronomy, Cambridge with financial support from the Science & Technology Facilities Council (STFC) and the European Research Council (ERC). It also made use of the Q3C software (Koposov & Bartunov 2006) and the SIMBAD data base (Wenger et al. 2000), operated at CDS, Strasbourg, France. This work has benefited from The UltracoolSheet at http://bit.ly/UltracoolSheet, maintained by Will Best, Trent Dupuy, Michael Liu, Aniket Sanghi, Rob Siverd, and Zhoujian Zhang, and developed from compilations by Dupuy & Liu (2012), Dupuy & Kraus (2013), Deacon et al. (2014), Liu et al. (2016), Best et al. (2018, 2021), Sanghi et al. (2023), and Schneider et al. (2023). We also used services and data provided by the Astro Data Lab (Fitzpatrick et al. 2014; Nikutta et al. 2020), which is part of the Community Science and Data Center (CSDC) Program of NSF NOIRLab. NOIRLab is operated by the Association of Universities for Research in Astronomy (AURA), Inc., under a cooperative agreement with the U.S. National Science Foundation.

LCS acknowledges support from UKRI-STFC grants ST/X001628/1 and ST/X001571/1. PWL acknowledges support by STFC grant ST/Y000846/1. SEK acknowledges support from the Science & Technology Facilities Council (STFC) grant ST/Y001001/1. JA-G acknowledges support from Fondecyt Regular 1201490 and by ANID–Millennium Science Initiative Program–ICN12_009 awarded to the Millennium Institute of Astrophysics MAS. DM gratefully acknowledges support from the Center for Astrophysics and Associated Technologies CATA by the ANID BASAL projects ACE210002 and FB210003, by Fondecyt Project No. 1220724. JLS acknowledges support from the Royal Society (URF\R1\191555). RK acknowledges partial support from ANID's FONDECYT Regular grant #1240249 and ANID's Millennium Science Initiative through grants ICN12_009 and AIM23-0001, awarded to the Millennium Institute of Astrophysics (MAS). RKS acknowledges support from CNPq/Brazil through projects 308298/2022-5 and 421034/2023-8.

DATA AVAILABILITY

The VIRAC2 catalogue and the underlying image data are available from the ESO archive at https://archive.eso.org. The cross match of VIRAC2 to VIVACE is available from the journal online.

REFERENCES

Alonso-García J., Mateo M., Sen B., Banerjee M., Catelan M., Minniti D., von Braun K., 2012, AJ, 143, 70
Alonso-García J., et al., 2018, A&A, 619, A4
Alonso-García J. et al., 2021, A&A, 651, A47
Beamín J. C. et al., 2013, A&A, 557, L8
Benjamin R. A. et al., 2003, PASP, 115, 953
Benjamin R., Babler B., Churchwell E., Clarkson W., Kirkpatrick D., Meade M., Whitney B., 2015, GLIMPSE Proper: Mid-Infrared Observations of Proper Motion and Variability Towards Galactic Center, Spitzer Proposal ID 12023.
Benjamin R., Babler B., D'Onghia E., Clarkson W., Churchwell E., Kirkpatrick D., Zasowski G., Majewski S., 2016, Three Dimensional Stellar

Kinematics of the Galactic Bar and Disk: Where APOGEE Meets GLIMPSE, Spitzer Proposal ID 13117
Best W. M. J. et al., 2018, ApJS, 234, 1
Best W. M. J., Liu M. C., Magnier E. A., Dupuy T. J., 2021, AJ, 161, 42
Burgasser A. J., Reid I. N., Siegler N., Close L., Allen P., Lowrance P., Gizis J., 2007, in Reipurth B., Jewitt D., Keil K., eds, Protostars and Planets V. 427, preprint (arXiv.astro-ph/0602122)
Burningham B. et al., 2011, MNRAS, 414, L90
Burningham B. et al., 2013, MNRAS, 433, 457
Carnero Rosell A. et al., 2019, MNRAS, 489, 5301
Casagrande L., Schönrich R., Asplund M., Cassisi S., Ramírez I., Meléndez J., Bensby T., Feltzing S., 2011, A&A, 530, A138
Caselden D., Colin G., Lack L., Marocco F., Kirkpatrick J., Meisner A., 2020, in American Astronomical Society Meeting Abstracts #235. p. 274.18
Chambers K. C. et al., 2016, preprint (arXiv:1612.05560)
Chauvin G., Lagrange A. M., Dumas C., Zuckerman B., Mouillet D., Song I., Beuzit J. L., Lowrance P., 2004, A&A, 425, L29
Churchwell E. et al., 2009, PASP, 121, 213
Clarke J. P., Wegg C., Gerhard O., Smith L. C., Lucas P. W., Wylie S. M., 2019, MNRAS, 489, 3519
Contreras Ramos R. et al., 2017, A&A, 608, A140
Deacon N. R. et al., 2014, ApJ, 792, 119
Drew J. E. et al., 2014, MNRAS, 440, 2036
Ducourant C., Teixeira R., Chauvin G., Daigne G., Le Campion J. F., Song I., Zuckerman B., 2008, A&A, 477, L1
Dupuy T. J., Kraus A. L., 2013, Science, 341, 1492
Dupuy T. J., Liu M. C., 2012, ApJS, 201, 19
El-Badry K., Rix H.-W., Heintz T. M., 2021, MNRAS, 506, 2269
Faherty J. K. et al., 2016, ApJS, 225, 10
Fitzpatrick M. J. et al., 2014, in Peck A. B., Benn C. R., Seaman R. L., eds, Proc. SPIE Conf. Ser. Vol. 9149, Observatory Operations: Strategies, Processes, and Systems V. SPIE, Bellingham, p. 91491T
Flewelling H. A. et al., 2020, ApJS, 251, 7
Folkes S. L., Pinfield D. J., Kendall T. R., Jones H. R. A., 2007, MNRAS, 378, 901
Folkes S. L. et al., 2012, MNRAS, 427, 3280
Gagné J. et al., 2018, ApJ, 856, 23
Gentile Fusillo N. P. et al., 2021, MNRAS, 508, 3877
Golovin A., Reffert S., Vani A., Bastian U., Jordan S., Just A., 2024, A&A, 683, A33
González-Fernández C. et al., 2018, MNRAS, 474, 5459
Griffith R. L. et al., 2012, AJ, 144, 148
Griggio M., Libralato M., Bellini A., Bedin L. R., Anderson J., Smith L. C., Minniti D., 2024, A&A, 687, A94
Hewett P. C., Warren S. J., Leggett S. K., Hodgkin S. T., 2006, MNRAS, 367, 454
Husseiniova A., McGill P., Smith L. C., Evans N. W., 2021, MNRAS, 506, 2482
Irwin M. J., 1985, MNRAS, 214, 575
Irwin M. J. et al., 2004, VISTA data flow system: pipeline processing for WFCAM and VISTA. p. 411
Ivanov V. D. et al., 2013, A&A, 560, A21
Kaczmarek Z., McGill P., Evans N. W., Smith L. C., Wyrzykowski Ł., Howil K., Jabłońska M., 2022, MNRAS, 514, 4845
Kaczmarek Z., McGill P., Evans N. W., Smith L. C., Golovich N., Kerins E., Specht D., Dawson W. A., 2024, MNRAS, 529, 1308
Kirkpatrick J. D. et al., 2011, ApJS, 197, 19
Kirkpatrick J. D. et al., 2019, ApJS, 240, 19
Kirkpatrick J. D. et al., 2021, ApJS, 253, 7
Kirkpatrick J. D. et al., 2024, ApJS, 271, 55
Klüter J., Bastian U., Demleitner M., Wambsganss J., 2018, A&A, 620, A175
Koposov S., Bartunov O., 2006, in Gabriel C., Arviset C., Ponz D., Enrique S., eds, Astronomical Society of the Pacific Conference Series Vol. 351, Astronomical Data Analysis Software and Systems XV. Astron. Soc. Pac., San Francisco, p. 735
Kurtev R. et al., 2017, MNRAS, 464, 1247
Lépine S., 2005, AJ, 130, 1247
Lépine S., 2008, AJ, 135, 2177
Lewis J. R., Irwin M., Bunclark P., 2010, Pipeline Processing for VISTA. p. 91
Libralato M. et al., 2015, MNRAS, 450, 1664
Lindegren L. et al., 2018, A&A, 616, A2
Lindegren L. et al., 2021, A&A, 649, A2
Liu M. C., Dupuy T. J., Allers K. N., 2016, ApJ, 833, 96
Looper D. L., Kirkpatrick J. D., Burgasser A. J., 2007, AJ, 134, 1162
Lucas P. W. et al., 2010, MNRAS, 408, L56
Lucas P. W. et al., 2024, MNRAS, 528, 1789
Luhman K. L., 2014, ApJ, 781, 4
Luhman K. L., Sheppard S. S., 2014, ApJ, 787, 126
Luna A., Marchetti T., Rejkuba M., Minniti D., 2023, A&A, 677, A185
Luna A., Marchetti T., Rejkuba M., Leigh N. W. C., Alonso-García J., Valenzuela Navarro A., Minniti D., Smith L. C., 2024, MNRAS, 528, 5495
Mace G. N. et al., 2013, ApJS, 205, 6
Marois C., Macintosh B., Barman T., Zuckerman B., Song I., Patience J., Lafrenière D., Doyon R., 2008, Science, 322, 1348
McGill P., Smith L. C., Evans N. W., Belokurov V., Lucas P. W., 2019, MNRAS, 487, L7
Meisner A. M., Lang D., Schlegel D. J., 2018, AJ, 156, 69
Meisner A. M. et al., 2020a, ApJ, 889, 74
Meisner A. M. et al., 2020b, ApJ, 899, 123
Mejías A., Minniti D., Alonso-García J., Beamín J. C., Saito R. K., Solano E., 2022, A&A, 660, A131
Michalik D., Lindegren L., Hobbs D., 2015, A&A, 574, A115
Minniti D. et al., 2010, New Astron., 15, 433
Minniti D., Fernández-Trincado J. G., Gómez M., Smith L. C., Lucas P. W., Contreras Ramos R., 2021, A&A, 650, L11
Minniti D. et al., 2024, A&A, 683, A150
Molnar T. A., Sanders J. L., Smith L. C., Belokurov V., Lucas P., Minniti D., 2022, MNRAS, 509, 2566
von Neumann J., 1941, Ann. Math. Stat., 12, 367
von Neumann J., 1942, Ann. Math. Stat., 13, 86
Nieuwmunster N. et al., 2024, A&A, 685, A93
Nikutta R., Fitzpatrick M., Scott A., Weaver B. A., 2020, Astron. Comput., 33, 100411
Oliveros-Gomez N., Manjavacas E., Ashraf A., Bardalez-Gagliuffi D. C., Vos J. M., Faherty J. K., Karalidi T., Apai D., 2022, ApJ, 939, 72
Padmanabhan N. et al., 2008, ApJ, 674, 1217
Patten B. M. et al., 2006, ApJ, 651, 502
Peña Ramírez K., Smith L. C., Ramírez Alegría S., Chené A. N., González-Fernández C., Lucas P. W., Minniti D., 2022, MNRAS, 513, 5799
Phan-Bao N. et al., 2008, MNRAS, 383, 831
Prusti T. et al., 2016, A&A, 595, A1
Reylé C., 2018, A&A, 619, L8
Reylé C., Jardine K., Fouqué P., Caballero J. A., Smart R. L., Sozzetti A., 2021, A&A, 650, A201
Saito R. K. et al., 2024, A&A, 689, A148
Sanders J. L., 2023, MNRAS, 523, 2369
Sanders J. L., Smith L., Evans N. W., Lucas P., 2019, MNRAS, 487, 5188
Sanders J. L., Smith L., González-Fernández C., Lucas P., Minniti D., 2022a, MNRAS, 514, 2407
Sanders J. L., Matsunaga N., Kawata D., Smith L. C., Minniti D., Lucas P. W., 2022b, MNRAS, 517, 257
Sanders J. L., Kawata D., Matsunaga N., Sormani M. C., Smith L. C., Minniti D., Gerhard O., 2024, MNRAS, 530, 2972
Sanghi A. et al., 2023, ApJ, 959, 63
Saydjari A. K. et al., 2023, ApJS, 264, 28
Schapera N. et al., 2022, Res. Notes Am. Astron. Soc., 6, 189
Schechter P. L., Mateo M., Saha A., 1993, PASP, 105, 1342
Schlafly E. F. et al., 2018, ApJS, 234, 39
Schlegel D. J., Finkbeiner D. P., Davis M., 1998, ApJ, 500, 525
Schmidt S. J., West A. A., Hawley S. L., Pineda J. S., 2010, AJ, 139, 1808
Schneider A. C., Greco J., Cushing M. C., Kirkpatrick J. D., Mainzer A., Gelino C. R., Fajardo-Acosta S. B., Bauer J., 2016, ApJ, 817, 112
Schneider A. C., Munn J. A., Vrba F. J., Bruursema J., Dahm S. E., Williams S. J., Liu M. C., Dorland B. N., 2023, AJ, 166, 103

Seifahrt A., Reiners A., Almaghrbi K. A. M., Basri G., 2010, A&A, 512, A37
Skrutskie M. F. et al., 2006, AJ, 131, 1163
Smart R. L. et al., 2021, A&A, 649, A6
Smith L. et al., 2014, MNRAS, 443, 2327
Smith L. C. et al., 2015, MNRAS, 454, 4476
Smith L. C. et al., 2018, MNRAS, 474, 1826
Smith L. C. et al., 2021, MNRAS, 505, 1992
Sormani M. C. et al., 2022, MNRAS, 512, 1857
Stassun K. G., Torres G., 2021, ApJ, 907, L33
Stetson P. B., 1987, PASP, 99, 191
Stetson P. B., 1996, PASP, 108, 851
Sutherland W. et al., 2015, A&A, 575, A25
Taylor M. B., 2005, in Shopbell P., Britton M., Ebert R., eds, ASP Conf. Ser. Vol. 347, Astronomical Data Analysis Software and Systems XIV. Astron. Soc. Pac., San Francisco, p. 29
Terzan A., Bernard A., Fresneau A., Ju K. H., 1980, Academie des Sciences Paris Comptes Rendus Serie B Sciences Physiques, 290, 321
Vos J. M., Faherty J. K., Gagné J., Marley M., Metchev S., Gizis J., Rice E. L., Cruz K., 2022, ApJ, 924, 68
Welch D. L., Stetson P. B., 1993, AJ, 105, 1813
Wenger M. et al., 2000, A&AS, 143, 9
Werner M. W. et al., 2004, ApJS, 154, 1
Whitney B. et al., 2011, Deep GLIMPSE: Exploring the Far Side of the Galaxy, Spitzer Proposal ID #80074.
Wright E. L. et al., 2010, AJ, 140, 1868
Zhang Z. H. et al., 2017, MNRAS, 464, 3040
Zhang Z. H. et al., 2018, MNRAS, 480, 5447

SUPPORTING INFORMATION

Supplementary data are available at *MNRAS* online.

Table 6. Cross-matches of VIVACE sources to VIRAC2 sources.
Please note: Oxford University Press is not responsible for the content or functionality of any supporting materials supplied by the authors. Any queries (other than missing material) should be directed to the corresponding author for the article.

APPENDIX A: DETAILS OF VIRAC2β

For the astrometric calibration (Section 2.3): VIRAC2β used *Gaia* DR2 as a reference catalogue, where VIRAC2 used *Gaia* eDR3. The earlier version used a fixed 8 degree Chebyshev polynomial, where the final one used varying degrees. The version of DoPhot used for VIRAC2β did not output centroid uncertainties, so these were fitted against the scatter in the residuals to the astrometric calibration as an approximate function of magnitude. For VIRAC2, we modified DoPhot such that it output centroid uncertainties, which were then calibrated against *Gaia* eDR3.

For the main pipeline: since the centroid uncertainties were fairly unreliable estimates, uncertainties from five-parameter astrometric fits were scaled to set the reduced χ^2 to unity. Additionally, we employed no residual-over-error selection threshold during source position matching. For the final version of the pipeline, the centroid uncertainties (which at this stage were output by DoPhot and scaled to match the scatter seen during astrometric calibration) were much more reliable, hence we found it unnecessary to perform the scaling on the five-parameter astrometric fit uncertainties. We also found it was now useful to use a residual-over-error selection threshold to clean the positional matching.

For VIRAC2β, the default proper motion was taken as the mean of local field stars from VIRAC version 1.1 (see Smith et al. 2018; Sanders et al. 2019; Section 2.1). For VIRAC2, the default proper motion was taken from VIRAC2β data.

APPENDIX B: SOME FAILURE MODES IN PARALLAX SOLUTIONS

Here, we describe two cases where our parallax-based search for new nearby sources (see Section 4.1.3) produced initially promising candidates, based on visual inspection of images to confirm high proper motion, but the VIRAC2 parallax was soon found to be incorrect.

(1) VIRAC2 source 13071355014500 was confirmed as a high proper motion star, with the images in fact showing it to be a triple system comprising two relatively bright, blended sources and a fainter source $\sim$3″away. However, the VIRAC2 entries for this system showed that while all three sources have very similar proper motions, the other two components have smaller VIRAC2 parallaxes: 6.2 ± 1.0 mas and 6.7 ± 2.2 mas for sources 13071355002815 and 13071355010344, compared to 32.0 ± 3.6 mas for 13071355014500. The two smaller parallaxes are confirmed by *Gaia* DR3 ($\sim$5.6 mas in both cases), though *Gaia* does not list a parallax for 13071355014500. We deduce that the parallax fit was corrupted by blending in the case of 13071355014500, which is the fainter component of the blend.

(2) VIRAC2 source 13431779012483 showed a clear motion of 0.5 arcsec between 2010 and 2018, but we noted that the image profile of this source was symmetric in some images but slightly elongated in others. On inspecting plots of position versus time we saw that the overall trend in each case was not well fit by a straight line: there were signs of curvature and a distinct jump between 2012 and 2013. This source has an entry as a long period variable (LPV) star in the VIVACE catalogue of candidate periodic variable VIRAC2 sources (Molnar et al. 2022). We then noticed that the K_s light curve was correlated with the position versus time plots, i.e. brightness was related to position. This, along with the elongation of the source in some images, made clear that source 13431779012483 is a blend of an LPV and another star. It is possible that there is a significant proper motion for one of the pair, to account for the overall trend in position versus time, but the high VIRAC2 parallax ($\varpi \approx 46$ mas) is an artefact of the blending and variability. This candidate had UWE = 1.16, somewhat higher than most bona fide nearby stars.

APPENDIX C: TABLE SCHEMATA

Table C1. Field names, units, and descriptions for the source table. An example row is also given, that of the early L dwarf β Circini B (Smith et al. 2015). The *sourceid* field links to the time series table (see Table C2). This format is the same for both the main and reject tables.

Name	Units	Description	Example row
sourceid		Unique source identifier	15869033004249
astfit_epochs		Number of epochs used for astrometric solution	180
astfit_params		Number of astrometric solution parameters	5
duplicate		Flag indicating a likely duplicate entry	0
ref_epoch	yr	Astrometric reference epoch	2014.0
ra	deg	Right ascension	229.33928126317744
ra_error	mas	Uncertainty on right ascension	0.48293653887707855
de	deg	Declination	−58.85879996158586
de_error	mas	Uncertainty on declination	0.7933554229463711
parallax	mas	Trigonometric parallax	31.564542172410846
parallax_error	mas	Uncertainty on trigonometric parallax	0.9661602760068156
pmra	mas yr^{-1}	Proper motion in right ascension times cos(dec)	−94.70174133405408
pmra_error	mas yr^{-1}	Uncertainty on proper motion in right ascension times cos(dec)	0.34828527350530797
pmde	mas yr^{-1}	Proper motion in declination	−134.84857408202345
pmde_error	mas yr^{-1}	Uncertainty on proper motion in declination	0.34549854257712753
ra_de_corr		Correlation between ra and de	0.029712955
ra_parallax_corr		Correlation between ra and parallax	0.33010614
ra_pmra_corr		Correlation between ra and pmra	0.2891742
ra_pmde_corr		Correlation between ra and pmde	0.011853172
de_parallax_corr		Correlation between de and parallax	0.09001031
de_pmra_corr		Correlation between de and pmra	0.0033594724
de_pmde_corr		Correlation between de and pmde	−0.032637153
parallax_pmra_corr		Correlation between parallax and pmra	0.0373232
parallax_pmde_corr		Correlation between parallax and pmde	0.035907157
pmra_pmde_corr		Correlation between pmra and pmde	0.0013401698
chisq		Chi squared of astrometric fit	336.16397
uwe		Unit weight error of astrometric fit	0.9731088
phot_z_mean_mag	mag	Mean Z-band magnitude	16.75006
phot_z_std_mag	mag	Standard deviation of Z-band magnitude	0.021935267
phot_z_n_epochs		Number of Z-band epochs contributing to statistics	8
z_n_obs		Approximate number of Z-band observations	9
z_n_det		Number of Z-band detections	9
z_n_amb		Number of Z-band detections shared with another source	0
phot_y_mean_mag	mag	Mean Y-band magnitude	15.495929
phot_y_std_mag	mag	Standard deviation of Y-band magnitude	0.016722715
phot_y_n_epochs		Number of Y-band epochs contributing to statistics	10
y_n_obs		Approximate number of Y-band observations	11
y_n_det		Number of Y-band detections	11
y_n_amb		Number of Y-band detections shared with another source	0
phot_j_mean_mag	mag	Mean J-band magnitude	14.492317
phot_j_std_mag	mag	Standard deviation of J-band magnitude	0.011483114
phot_j_n_epochs		Number of J-band epochs contributing to statistics	5
j_n_obs		Approximate number of J-band observations	6
j_n_det		Number of J-band detections	6
j_n_amb		Number of J-band detections shared with another source	0
phot_h_mean_mag	mag	Mean H-band magnitude	13.750394
phot_h_std_mag	mag	Standard deviation of H-band magnitude	0.014054991
phot_h_n_epochs		Number of H-band epochs contributing to statistics	5
h_n_obs		Approximate number of H-band observations	6
h_n_det		Number of H-band detections	6
h_n_amb		Number of H-band detections shared with another source	0
phot_ks_mean_mag	mag	Mean K_s-band magnitude	13.21982
phot_ks_std_mag	mag	Standard deviation of K_s-band magnitude	0.019139782
phot_ks_n_epochs		Number of K_s-band epochs contributing to statistics	141
ks_n_obs		Approximate number of K_s-band observations	184
ks_n_det		Number of K_s-band detections	180

Table C1 – *continued*

Name	Units	Description	Example row
ks_n_amb		Number of K_s-band detections shared with another source	0
ks_first_epoch	MJD	Epoch of first K_s-band detection	55260.36375826
ks_last_epoch	MJD	Epoch of last K_s-band detection	58717.06490433
ks_skew		Skewness of K_s-band magnitudes	0.6108212
ks_p0	mag	0th percentile (i.e. min) of K_s-band magnitudes	13.172082
ks_p1	mag	1st percentile of K_s-band magnitudes	13.1780205
ks_p2	mag	2nd percentile of K_s-band magnitudes	13.185369
ks_p4	mag	4th percentile of K_s-band magnitudes	13.191636
ks_p5	mag	5th percentile of K_s-band magnitudes	13.193609
ks_p8	mag	8th percentile of K_s-band magnitudes	13.197648
ks_p16	mag	16th percentile of K_s-band magnitudes	13.20169
ks_p25	mag	25th percentile of K_s-band magnitudes	13.206783
ks_p32	mag	32nd percentile of K_s-band magnitudes	13.210841
ks_p50	mag	50th percentile (i.e. median) of K_s-band magnitudes	13.217017
ks_p68	mag	68th percentile of K_s-band magnitudes	13.2265835
ks_p75	mag	75th percentile of K_s-band magnitudes	13.231348
ks_p84	mag	84th percentile of K_s-band magnitudes	13.238225
ks_p92	mag	92nd percentile of K_s-band magnitudes	13.245653
ks_p95	mag	95th percentile of K_s-band magnitudes	13.2479105
ks_p96	mag	96th percentile of K_s-band magnitudes	13.249347
ks_p98	mag	98th percentile of K_s-band magnitudes	13.267736
ks_p99	mag	99th percentile of K_s-band magnitudes	13.27843
ks_p100	mag	100th percentile (i.e. max) of K_s-band magnitudes	13.288555
ks_mad	mag	MAD from the median K_s-band magnitude	0.012143135
ks_med_err	mag	Median uncertainty of K_s-band magnitudes	0.0201695
ks_Stetson_I		Stetson I index for K_s-band magnitudes	0.21573663035284185
ks_Stetson_J		Stetson J index for K_s-band magnitudes	0.13496087363194595
ks_Stetson_K		Stetson K index for K_s-band magnitudes	0.8183742496792374
ks_Stetson_group_count		Number of observation groups used for Stetson indices	61
ks_eta		von Neumann eta index	1.5645293017153363
ks_eta_f		Modified von Neumann eta index	1051447886.8728735

Table C2. Field names, units and descriptions for the time series table. An example row is also given, that of the first time series element for the example source shown in Table C1. The *sourceid* field links to the source table (see Table C1), and the *catid* field links to the observation table (see Table C3). This format is the same for both the main and reject tables.

Name	Units	Description	Example row
sourceid		Unique source identifier	15869033004249
catid		Unique observation identifier	120741
mjdobs	MJD	Epoch of observation	55260.36375826
filter		Observation bandpass name	K_s
seeing	arcsec	Observation seeing	0.624116289
ra	deg	Right ascension	229.33949898506464
de	deg	Declination	−58.85866266424065
era	mas	Error on right ascension	7.892984765147925
edec	mas	Error on declination	9.436603552353597
mag	mag	Magnitude	13.245622
emag	mag	Error on magnitude	0.021564407
phot_flag		Photometric error flag	0
x	pixel	Detector X-position	1152.587
y	pixel	Detector Y-position	918.431
ex	pixel	Error on detector X-position	0.023
ey	pixel	Error on detector Y-position	0.02
cnf_ctr		CASU confidence value of centroid pixel	95
chi		dophot chi of detection	2.52
objtype		dophot object type	1
ext		VIRCAM detector number	13
ast_res_chisq		Chi squared of astrometric residual	4.3247724
ambiguous_match		Flag indicating shared detection	0

Table C3. Field names, units and descriptions for the observation index table. An example row is also given, that of the observation corresponding to the time series element shown in Table C2. The *catid* field links to the time series table (see Table C2).

Name	Units	Description	Example row
catid		Unique observation identifier	120741
filename		FITS filename of the image	v20100304_00780_st.fits.fz
tile		VVV tile name	d018
ob		OB name	d018v-1
filter		Filter name	K_s
ra	deg	Right ascension	228.858112
de	deg	Declination	−59.48647
l	deg	Galactic longitude	320.302109749199
b	deg	Galactic latitude	−1.56127378157683
exptime	s	Exposure time	4.0
mjdobs	MJD	MJD of observation	55260.36375826
airmass		Airmass	1.222
skylevel		Sky level (CASU)	4981.22
skynoise		Sky noise (CASU)	45.515
elliptic		Ellipticity (CASU)	0.10192925
seeing	arcsec	Seeing	0.624116289

APPENDIX D: UCD FINDER CHARTS

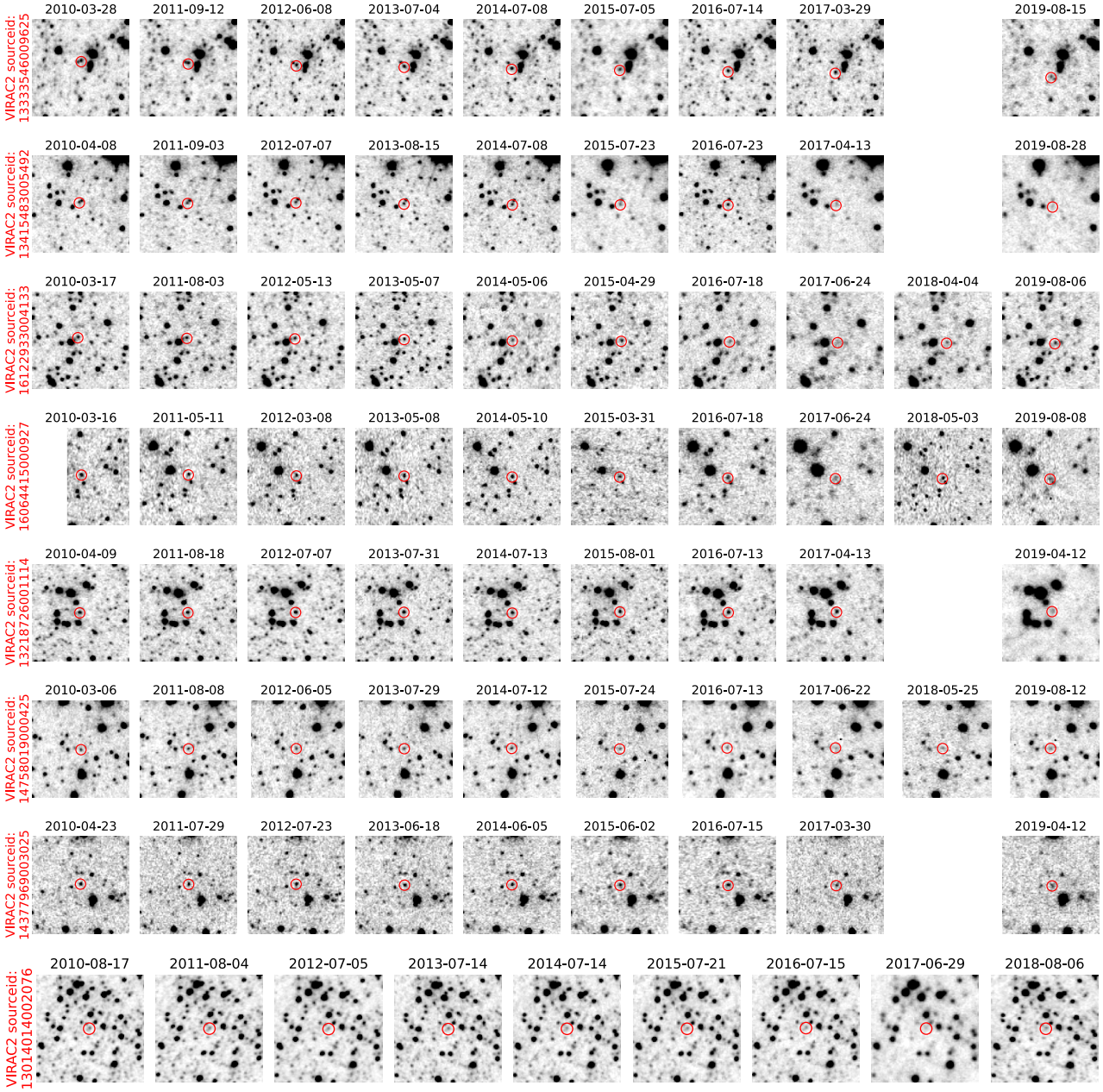

Figure D1. Finder charts, one per calendar year, for eight of the more interesting UCD candidates from Section 4.1. The charts are centred on the VIRAC2 2014.0 position of each target, they are 30 arcsec in size, north is up and east is to the left. From top to bottom, the targets are: VVV J1814-2654, VVV 1820-2742, VVV 1253-6339, VVV J1210-6227, VVV J1728-2543, VVV J1705-4245, VVV J1754-3813, and VVV J1759-2340. The red circle in each panel indicates the location of the target at that epoch, taking the VIRAC2 proper motion and parallax into account.

This paper has been typeset from a TEX/LATEX file prepared by the author.